iScience

CellPress

Article

Anomalous Dense Liquid Condensates Host the Nucleation of Tumor Suppressor p53 Fibrils

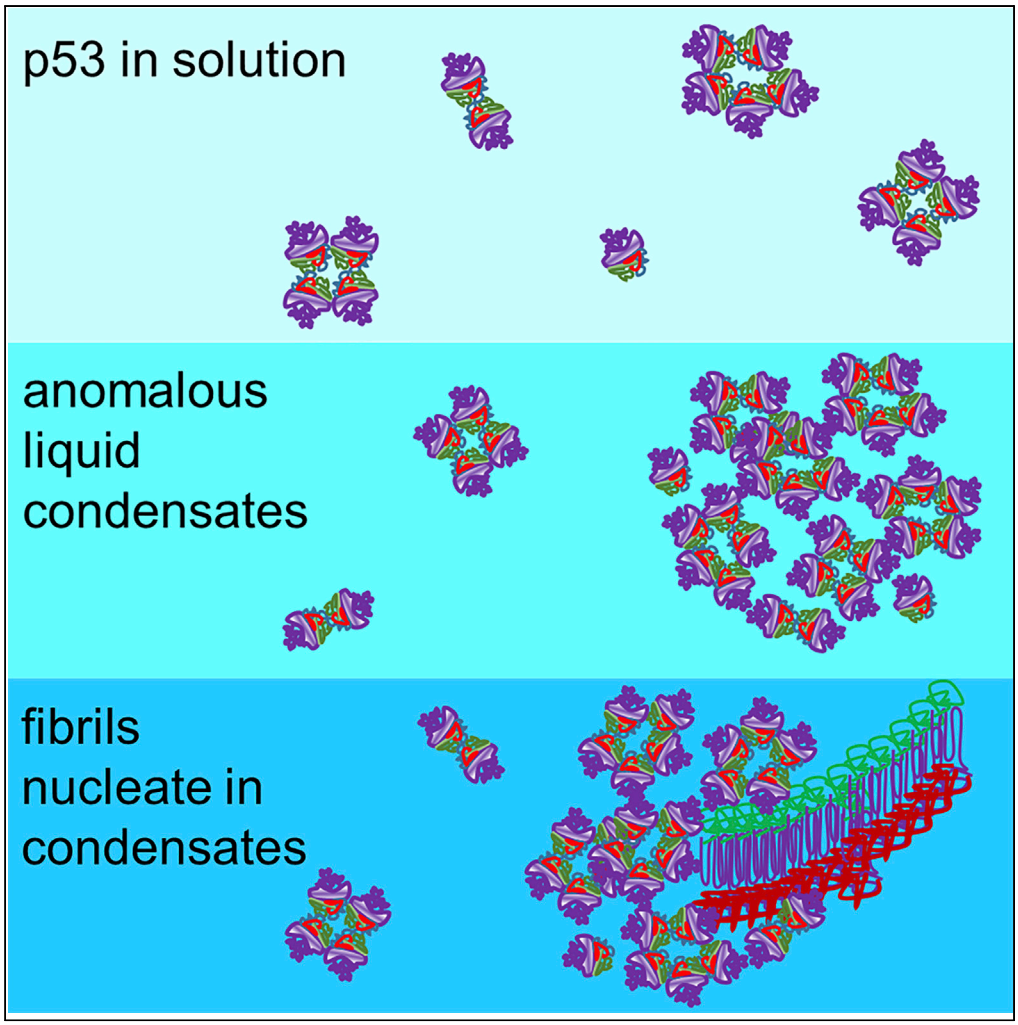

Mohammad S. Safari, Zhiqing Wang, Kunaal Tailor, Anatoly B. Kolomeisky, Jacinta C. Conrad, Peter G. Vekilov

tolya@rice.edu (A.B.K.)
jcconrad@uh.edu (J.C.C.)
vekilov@uh.edu (P.G.V.)

HIGHLIGHTS

Wild-type p53 forms anomalous liquid-phase condensates

The condensates are distinct from dense liquids seen with other proteins

The condensates serve as precursors for p53 fibril assembly

Fibril nucleation hosted by liquid precursors is an unexplored biological pathway

Safari et al., iScience *12*, 342–355
February 22, 2019
https://doi.org/10.1016/j.isci.2019.01.027

iScience

CellPress

Article

Anomalous Dense Liquid Condensates Host the Nucleation of Tumor Suppressor p53 Fibrils

Mohammad S. Safari,[1,2] Zhiqing Wang,[1] Kunaal Tailor,[1] Anatoly B. Kolomeisky,[3,*] Jacinta C. Conrad,[1,*] and Peter G. Vekilov[1,4,5,*]

SUMMARY

About half of human cancers are associated with mutations of the tumor suppressor p53. Gained oncogenic functions of the mutants have been related to aggregation behaviors of wild-type and mutant p53. The thermodynamic and kinetic mechanisms of p53 aggregation are poorly understood. Here we find that wild-type p53 forms an anomalous liquid phase. The liquid condensates exhibit several behaviors beyond the scope of classical phase transition theories: their size, ca. 100 nm, is independent of the p53 concentration and decoupled from the protein mass held in the liquid phase. Furthermore, the liquid phase lacks constant solubility. The nucleation of p53 fibrils deviates from the accepted mechanism of sequential association of single solute molecules. We find that the liquid condensates serve as pre-assembled precursors of high p53 concentration that facilitate fibril assembly. Fibril nucleation hosted by precursors represents a novel biological pathway, which opens avenues to suppress protein fibrillation in aggregation diseases.

INTRODUCTION

Liquid-liquid phase separation constitutes the formation pathway of several common organelles such as nucleoli, Cajal bodies, and P granules, which are not delimited by membranes (Uversky, 2017; Wei et al., 2017). The condensates generated by phase separation are thought to concentrate biological reactants and to coordinate responses to environmental stress, among other functions (Shin and Brangwynne, 2017). A fundamental open question concerns the mechanism and consequences of the transition of the liquid condensates into ordered or disordered solids (Shin and Brangwynne, 2017), which may be associated with the growing class of aggregation diseases, such as sickle cell disease, Alzheimer disease, and diabetes mellitus type 2 (Aguzzi and O'Connor, 2010; Kato et al., 2018; Knowles et al., 2014).

The transcription factor p53, one of the most important tumor suppressors, transforms after mutation into a powerful cancer promoter that blocks the anti-cancer activity of wild-type p53, its paralogs p63 and p73, and other distinct anti-cancer pathways (Bieging et al., 2014; Joerger and Fersht, 2016). Several mechanisms of the gain of oncogenic function (GOF) of mutant p53 have been proposed (Muller and Vousden, 2013). Malignant mutations that destabilize the p53 conformation enhance its fibrillation (Ang et al., 2006; Olivier et al., 2002). The mutants' co-aggregation with wild-type p53 and its paralogs has been recognized as a potent GOF mechanism (Costa et al., 2016; Xu et al., 2011). Fibril suppression, for instance, by stabilization of the mutant p53 conformation, has been identified as a general way to fight cancer (Joerger and Fersht, 2016; Soragni et al., 2016). Accordingly, cancer has been defined, in certain respect, as an aggregation-related disease (Costa et al., 2016; Xu et al., 2011).

The aggregation of mutant and wild-type p53, *in vitro* and *in vivo*, exhibits features typical of β-amyloid fibrillation. The amyloid domains bind to thioflavin T (ThT), a fluorescent dye that recognizes β-aggregates, and the fluorescence intensity increases following a typical sigmoid curve (Costa et al., 2016; Wang and Fersht, 2017; Wilcken et al., 2012; Xu et al., 2011). Other characteristics of p53 fibrillation have provoked questions on the molecular mechanisms. Notably, the concentration independence of the parameters of the sigmoid curve and the short initial time period have suggested that a "non-classical mechanism" of fibril nucleation and growth operates (Wang and Fersht, 2017; Wilcken et al., 2012). Tests of whether mutant p53 fibrils cross-seed wild-type aggregation have produced both positive and negative outcomes (Wang and Fersht, 2015; Xu et al., 2011). Furthermore, the significance of intracellular crowding for the kinetics of

[1]Department of Chemical and Biomolecular Engineering, University of Houston, 4726 Calhoun Road, Houston, TX 77204-4004, USA

[2]Department of Molecular Biology, Princeton University, Princeton, NJ 08544-1014, USA

[3]Department of Chemistry, Rice University, P.O. Box 1892, MS 60, Houston, TX 77251-1892, USA

[4]Department of Chemistry, University of Houston, 3585 Cullen Boulevard, Houston, TX 77204-5003, USA

[5]Lead Contact

*Correspondence: tolya@rice.edu (A.B.K.), jcconrad@uh.edu (J.C.C.), vekilov@uh.edu (P.G.V.)

https://doi.org/10.1016/j.isci.2019.01.027

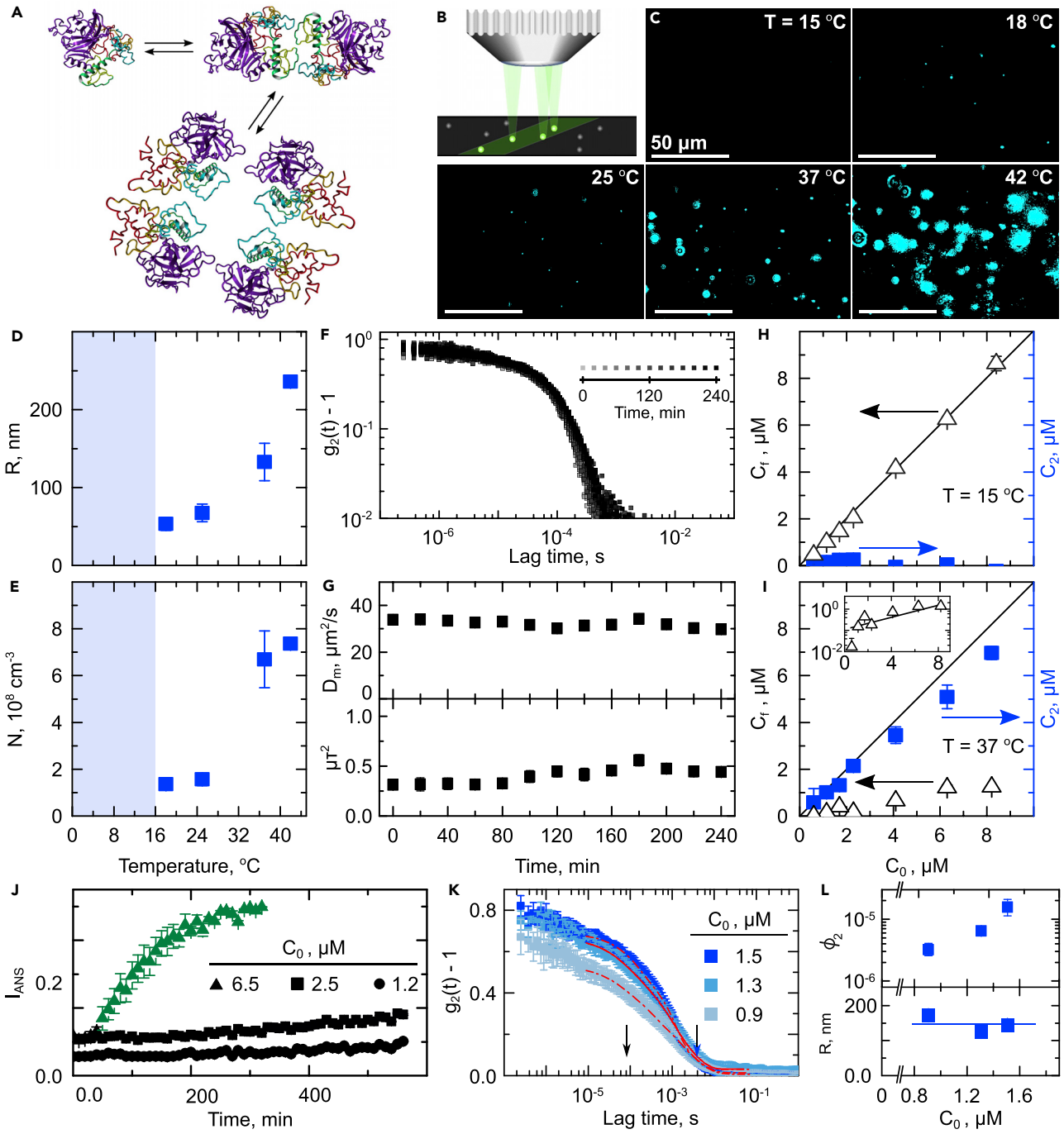

Figure 1. Anomalous p53 Liquid Condensates

(A) The structure of p53. The transactivation domain (TAD, 1–61), proline-rich region (PRR, 61–94), DNA-binding domain (DBD, 94–292), and oligomerization domain (OD, 325–356) are colored red, gold, purple, and green, respectively. TAD and PRR are intrinsically disordered; DBD and OD are structured. p53 is a homotetramer that readily decays to dimers.

(B) Schematic of oblique illumination microscopy (OIM). A green laser illuminates a thin solution layer at an oblique angle. The light scattered by particles in the solution is collected by a microscope lens.

(C) Representative OIM micrographs collected from a p53 solution with concentration C_0 = 2.2 μM after incubation for 20 min at each temperature. The observed volume is 5 × 80 × 120 μm^3 depth × height × width. Aggregates appear as cyan speckles.

(D and E) (D) The average radius R and (E) the total number N of the aggregates, determined by OIM from (C). The average of five determinations in distinct solution volumes is shown. Error bars indicate standard deviations. Temperature range where aggregation is not observed is shaded.

(F) Intensity correlation functions g_2 of the light scattered by a filtered p53 solution with C_0 = 6 μM at 15°C acquired at different times.

Figure 1. *Continued*

(G) Evolution of diffusivity D_m and dispersity $\mu\tau^2$ of unaggregated p53 evaluated from the g_2s in (F). The error bars are generated from four distinct g_2s and are smaller than the symbols.

(H and I) Concentration of p53 after incubation for 20 min at (H) 15°C and (I) 37°C, as a function of the initial solution concentration C_0. △, the concentration of the p53 solution C_f after filtration to remove aggregates. ■, concentration C_2 of p53 incorporated into aggregates, evaluated as $C_2 = C_0 - C_f$. Error bars indicate standard deviations of three measurements on one sample.

(J) Evolution of the intensity of fluorescence at 490 nm of 1-anilino-8-naphthalenesulfonate (ANS) in the presence of p53 at concentrations listed on the plot at 37°C. Error bars indicate standard deviations of two measurements on one sample. Green color denotes signal attributed to fibrils.

(K) Intensity correlation functions g_2 of unfiltered p53 solutions. Solution at 1.5 μM was incubated at 37°C for 4 h and serially diluted to 1.3 and 0.9 μM. Ten g_2s were averaged at each concentration, and the error bars represent the standard deviation.

(L) The dependence of anomalous liquid volume ϕ_2, and the average radius R of the condensates on the protein concentration evaluated from g_2s in (K). The error bars are generated from four distinct g_2s and are smaller than the symbols for R. Horizontal line designates the average R = 145 nm.

fibril nucleation and growth is incompletely understood. In cells, p53 localizes in the nucleus, in which DNA, protein complexes, RNAs, and multiple other types of biomolecules occupy up to 50% of the total volume and significantly modify protein folding, stability, and aggregation (van den Berg et al., 2017).

To address these questions, we explore the aggregation of wild-type p53 at near-physiological conditions and in crowded environments. Besides serving as a reference for mutant p53 behaviors, aggregation of wild-type p53 is of interest because it may, under certain conditions, behave like mutant p53 (Muller and Vousden, 2013). Wild-type p53 has been detected in a mutant conformation in hypoxic cells (Gogna et al., 2012) and after binding to a p53 regulator protein, MDM2 (Sasaki et al., 2007). We demonstrate a non-classical nucleation mechanism of p53 fibrils, whereby anomalous p53 liquid condensates serve as pre-assembled precursors that host fibril assembly. We establish the kinetic and thermodynamic laws that govern the formation and decay of p53 condensates and demonstrate that they deviate from the classical laws of phase separation that also govern the formation of dense protein liquids (Shin and Brangwynne, 2017; Uversky, 2017; Wei et al., 2017); this disparity identifies the p53 condensate as a new class of liquid.

RESULTS

Detection and Identification of p53 Liquid Condensates

Oblique illumination microscopy (OIM, Figure 1B and Video S1) (Vorontsova et al., 2015a) revealed that the aggregation of p53 strongly depends on temperature (Figure 1C). (For purification procedures and p53 identification, see Figures S1 and S2.) Solutions incubated at 15°C for 20 min contain no visible aggregates. On the contrary, solutions kept at 18°C and 25°C contain a few aggregates; pronounced aggregation is observed in solutions heated to 37°C and 42°C. The average radius R and the number N of the aggregates both increase nonlinearly with temperature (Figures 1D and 1E). The remarkable growth in size and number of these aggregates at temperatures approaching 42°C (Figures 1D and 1E), the mid-denaturation point of p53 (Bell et al., 2002), suggests that unfolding of p53 may be an essential trigger for aggregation.

To elucidate the mechanism of the aggregates detected in Figure 1C, we started with solutions of unaggregated protein. We removed possible aggregates by filtration and characterized unaggregated p53 at 15°C by dynamic light scattering (DLS). The intensity-intensity correlation functions of the filtrate revealed a broad shoulder (Figure 1F), indicating the presence of distinct scatterers. The characteristic decorrelation time of that shoulder, 90 μs, corresponds to an average diffusivity $D_m = 32\ \mu m^2 s^{-1}$ (Figure 1G), which relates (by the Stokes-Einstein law $D_m = k_B T/6\pi\eta R_m$, where $k_B T$ is the thermal energy, $\eta = 1.5$ mPa•s is the independently measured solvent viscosity, and R_m is the molecular radius) to an average $R_m = 6$ nm, higher than the ca. 4 nm radius expected for a p53 tetramer of molecular weight 175 kg mol^{-1} (Chalkey et al., 1994). Consonantly with the exaggerated radius, the considerable polydispersity $\mu\tau^2 \approx 0.35$ (Figure 1G) indicates the presence of higher-order oligomers (Rajagopalan et al., 2011; Xu et al., 2011). Both D_m and $\mu\tau^2$ remained steady over time at 15°C.

To determine whether the aggregates detected in Figure 1C are droplets of dense p53 liquid, we measured the concentration of p53 in equilibrium with the aggregate phase, C_f. We incubated solutions at 15°C and 37°C for 20 min and removed the aggregates by filtration. After incubation at 15°C, C_f was nearly identical to the initial concentration C_0 (Figure 1H), confirming the lack of aggregates at this temperature (Figure 1C). In solutions incubated at 37°C, however, C_f was sharply lower than C_0, with aggregates capturing up to 80% of the total p53 (Figure 1I). Surprisingly, C_f was not constant, but instead increased exponentially with C_0 (inset of Figure 1I). The finding of increasing terminal concentration is in striking contrast with examples

of dense protein liquids, which equilibrate with solutions of constant concentration (Broide et al., 1991; Chen et al., 2004; Galkin et al., 2002; Muschol and Rosenberger, 1997; Uversky, 2017; Wei et al., 2017).

Earlier studies reported the formation of p53 amyloid structures (Ang et al., 2006; Costa et al., 2016; Wang and Fersht, 2017; Wilcken et al., 2012; Xu et al., 2011) at 37°C. Similar to dense liquids but in contrast to the aggregates characterized in Figures 1C–1E and 1I, amyloid fibrils exhibit solubility, which is independent of the initial solution concentration (Qiang et al., 2013). To further assess whether the p53 aggregates are amyloid fibrils, we employed the 1-anilino-8-naphthalenesulfonate (ANS) assay. ANS emits fluorescence at 500 nm when it associates with exposed hydrophobic sites of partially unfolded protein segments and amyloid fibrils (Hawe et al., 2008). The pronounced ANS fluorescence intensity immediately after introduction in the solution (Figure 1J) indicates the presence of misfolded segments that may correspond to the intrinsically disordered transactivation domain (TAD) and proline-rich region (PRR) domain of p53 (Figure 1A). The fluorescence intensity was steady for ca. 40 min at 37°C (Figure 1J) and ca. 200 min at 15°C and then ascended, suggesting inception of amyloid fibrillation likely due to misfolding of the structured DNA-binding domain (DBD) and oligomerization domain (Figure 1A; Wang and Fersht, 2017; Wilcken et al., 2012). The observed fibrillation delay is likely due to slow nucleation (Wang and Fersht, 2017; Wilcken et al., 2012); importantly, it indicates that the aggregates observed in Figure 1C after 20 min incubation at temperatures in the range 18°C–37°C are not amyloids.

The reversibility of these aggregates, demonstrated by the light scattering results in Figures 1K and 1L, indicates that they are not disordered agglomerates either. Indeed, the intensity-intensity correlation functions g_2 (Figure 1K) reveal two shoulders, corresponding to the diffusion of two scatterers with characteristic times ca. 100 μs and 10 ms. The fast scatterers are likely the p53 oligomers detected in the filtered solutions at 15°C (Figure 1K). The average radius of the large scatterers, 145 nm, is similar to the aggregate radius revealed by OIM at this temperature, 37°C (Figure 1D). The relative volume of the condensate population ϕ_2, evaluated from g_2 (Pan et al., 2007), is a sensitive function of the p53 concentration (Figure 1L): 1.7-fold dilution of C_0 induces ca. 8× reduction of ϕ_2. The strong dependence of ϕ_2 on C_0 is a manifestation of the condensate reversibility, rarely observed for disordered agglomerates.

The lack of dependence of the aggregate size R on C_0 and its decoupling from the volume of the aggregate phase ϕ_2 distinguish the observed structures from common protein condensate phases, such as crystals, amyloid fibrils, dense liquids, and amorphous precipitates. In further divergence from classical phase behaviors, these condensates did not display constant solution concentration at equilibrium. For all common protein assemblies, the equilibrium protein concentration in the supernatant is constant and independent of the initial concentration (Asherie et al., 1998; Chernov and Komatsu, 1995; Fabry et al., 2001; Safari et al., 2017; Thomson et al., 1987). Furthermore, the size of these assemblies after equilibration, measured as fibril length, crystal width, or droplet radius, grows concurrently with the initial solution concentration as an implementation of the law of mass action (Chaikin and Lubensky, 1995; van Raaij et al., 2008).

Unlike these typical aggregates, the size of the observed p53 condensates was independent of the p53 concentration, and the volume of the condensate phase increased with C_0 (Figure 1L). These unusual behaviors have been previously reported for abnormal liquid condensates of several proteins (Gliko et al., 2005; Li et al., 2012; Schubert et al., 2017; Sleutel and Van Driessche, 2014; Yamazaki et al., 2017). We conclude that the anomalous condensates detected in Figure 1 represent clusters of abnormal p53 liquid.

The Anomalous p53 Liquid Condensates in Crowded Solutions

For further insight into the properties and mechanisms of the anomalous p53 liquid condensates, we examined their behaviors upon addition of a crowding agent. We chose Ficoll 70 kDa, a cross-linked compact polysaccharide with radius 4.7 nm (Georgalis et al., 2012) and concentrations up to 90 mg mL^{-1}, which occupies ca. 35% of the solution volume, to mimic the conditions inside cells. OIM revealed that p53 condensation was boosted when Ficoll was added to solutions (Figure 2A and Video S2). Condensation was enhanced likely because crowding amplified the driving force for reactions that reduce the reactant volume, such as aggregation (Ellis and Minton, 2003). The average size of the condensates, 80–90 nm, was independent of the p53 concentration (Figure 2B), analogously to the behavior in uncrowded solutions (Figure 1L), and also of the Ficoll concentration (Figure 2C). By contrast, the amount of p53 in the condensates increased at higher initial concentration of the solution (Figure 2D). The amount of decoupled p53 in the condensates and the condensate size highlights the similarity to the behavior of anomalous p53 liquid condensates existing in uncrowded p53 solutions (Figure 1).

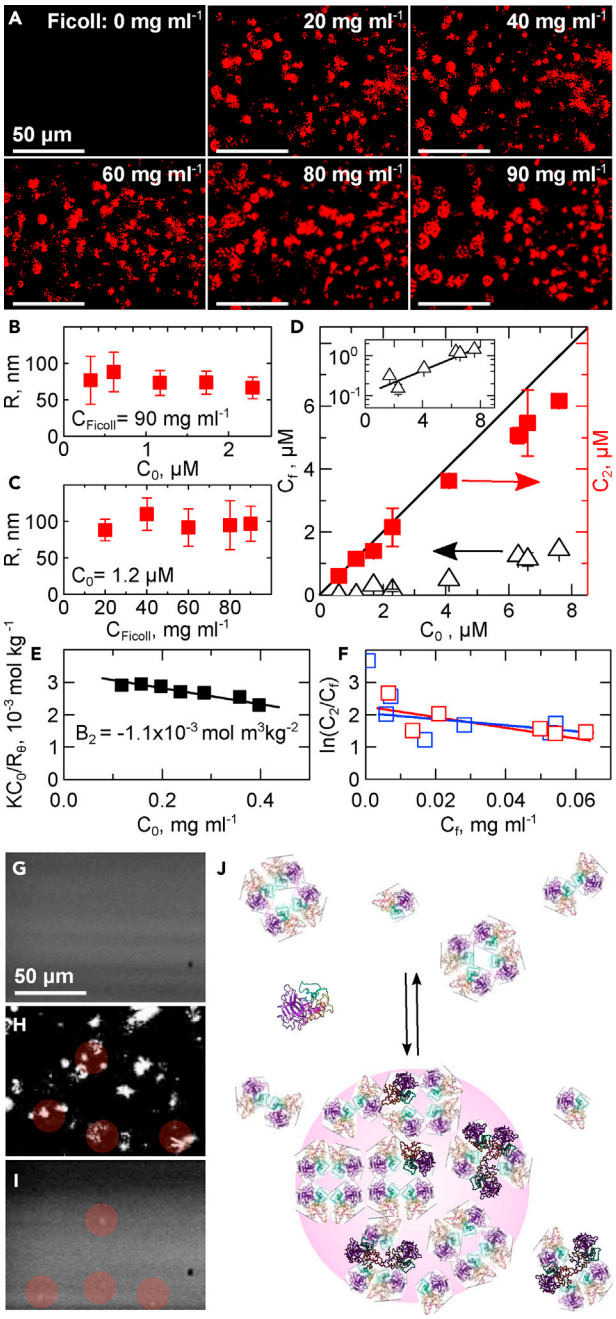

Figure 2. p53 Condensates in Crowded Solutions

(A) Representative OIM micrographs collected immediately after addition of crowders to a p53 solution with C_0 = 1.2 μM held for 20 min at T = 15°C. Ficoll concentration is listed in each image. The observed volume is 5 × 80 × 120 μm^3. Condensates appear as red spots.

(B and C) The average radius of the condensates *R* as a function of (B) p53 and (C) Ficoll concentrations, determined by OIM. The average of five determinations in distinct solution volumes is shown. Error bars indicate standard deviations. The high number of condensates prevents their accurate count by OIM.

(D) Concentration of p53 after incubation for 20 min at 15°C in the presence of 56 mg mL^{-1} Ficoll as a function of the initial solution concentration C_0. △, the concentration of p53 solution C_f after filtration to remove condensates. ■, concentration of p53 incorporated into the anomalous liquid, evaluated as $C_2 = C_0 - C_f$. Error bars indicate standard deviations of three measurements on one sample.

Figure 2. *Continued*

(E) The osmotic compressibility of the solution KC_0/R_θ (K, instrument constant; R_θ, Rayleigh ratio of the intensity of light scattered at angle $\theta = 90°$ to that of incident light) as a function of C_0 at 15°C. The value of the second osmotic virial coefficient B_2 evaluated from the slope of the data is displayed.

(F) The correlation between $\ln(C_2/C_f)$ and C_f in crowded solutions at 15°C (red) and uncrowded solutions at 37°C (blue) from data in, respectively, Figures 2D and 1I.

(G) Fluorescence OIM image of 15 mg mL^{-1} boron-dipyrromethene- (BODIPY)-labeled Ficoll.

(H) OIM micrograph of same solution after addition of 1.2 μM p53.

(I) Fluorescence OIM micrograph of the same solution volume as in (H) taken within 1 min of (H). Red circles in (H) and (I) highlight condensates containing BODIPY-labeled Ficoll.

(J) Schematic of the formation of anomalous p53 liquid condensates owing to the dynamics of formation, decay, and diffusion of transient misassembled oligomers, tentatively represented as pentamers that are hypothesized to form in the solution in addition to the long-lived monomers, dimers, and tetramers.

The current theory of anomalous protein liquid condensates suggests that transient protein complexes such as dimers, for single-chain proteins, or misassembled oligomers, for oligomeric proteins, accumulate in the condensate core (Chan et al., 2012; Pan et al., 2010; Vorontsova et al., 2015a). In this model, the condensate size is determined by the balance between the lifetime of the complexes and their rate of outward diffusion from the condensate and is, hence, independent of the protein concentration and the other thermodynamic parameters of the solution (Pan et al., 2010; Safari et al., 2017). By contrast, the amount of protein captured in the condensates increases exponentially with the protein concentration as a consequence of a thermodynamic equilibrium between the condensates and the bulk solution (Li et al., 2012; Pan et al., 2010).

The presence of misassembled oligomers in p53 solutions is attested by the exaggerated size and significant polydispersity of unaggregated p53 (Figure 1G). It is feasible that one or more of the misassembled oligomers (distinct from the long-lived dimers and tetramers; Rajagopalan et al., 2011) would have lifetimes of the order 100 μs that underlie condensates of size ca. 100 nm (Chan et al., 2012). To test the applicability of two tenets of the anomalous protein liquid model to the p53 condensates, namely, the anomalous liquid is enriched in p53 oligomers distinct from the majority tetramers and is in equilibrium with the solution, we examined the striking quasi-exponential dependence of the equilibrium solution concentration C_f on its initial value C_0 in both crowded and uncrowded solutions (Figures 2D and 1I).

Thermodynamic analysis discussed in the Supplemental Information accounts for the distinctive composition of the condensates by positing that the modified standard chemical potential of p53 captured in them, ψ_2, differs from that in the solution μ_1°. In defining μ_1°, we ignore the polydispersity of the p53 oligomers. We account for the solution nonideality due to interactions between the p53 solute molecules by introducing an activity coefficient γ as $ln\gamma = 2B_2M_wC_f$, where B_2 is the second osmotic virial coefficient and M_w is the p53 molecular weight. Assuming equilibrium, $\mu_1 = \mu_2$, the concentration of p53 captured in the condensates is given by $C_2 = C_f \exp\left(-\frac{\psi_2 - \mu_1^0}{RT}\right)\exp(2B_2M_wC_f)$. This relation predicts that C_f increases quasi-exponentially with $C_0 = C_2 + C_f$ (Figure S5) and C_2/C_f should be an exponential function of C_f with exponent related to B_2.

To test this prediction, we determined B_2 of the p53 solution by static light scattering (Berne and Pecora, 2000). This analysis yielded average molecular weight $M_w = 303$ kg mol^{-1} and $B_2 = -1.1\times10^{-3}$ mol m^3 kg^{-2} (Figure 2E). The value of M_w, about 2-fold that of the p53 tetramer, indicates the presence of higher-order misassembled oligomers in the solution, consistent with the high polydispersity of p53 solutions and the slow diffusion of unaggregated p53 observed with DLS (Figure 1G). The considerable negative value of B_2 indicates strong effective attraction between p53 molecules. Correspondingly, the slopes of $ln(C_2/C_f)$ as a function of C_f (Figure 2F) were negative in both crowded and uncrowded solutions. The slopes of the correlations between $ln(C_2/C_f)$ and C_f, 10.0 and 14.0 m^3 kg^{-1} (Figure 2F), are significantly greater than the product $2B_2M_w = 0.66$ m^3 kg^{-1}. This discrepancy is likely due to the lower magnitude of B_2, determined at 15°C in uncrowded solutions, than at 37°C or in the presence of Ficoll, the conditions at which the behaviors depicted in Figure 2F were recorded. Higher temperature destabilizes the conformation of the ordered p53 domains, which increases the protein hydrophobicity and its contribution to intermolecular attraction. Similarly, the enhanced aggregation propensity in crowded solutions is equivalent to effective attraction. Both factors lead to significantly greater magnitude of B_2. Determinations of B_2 in the presence of Ficoll or at 37°C were obstructed by the aggregation of p53 (Figures 1C and 2A). The intercepts of the straight lines in Figure 2F are 2.33 and 1.85, suggesting that ψ_2 is lower than μ_1^0 by ca. 5 kJ mol^{-1}. The higher stability of the anomalous liquid is consistent with the high fraction of protein captured in it.

To test whether Ficoll infiltrates the anomalous liquid condensates, we examined by OIM solutions of fluorescently labeled Ficoll with and without p53. We observed that p53 condensates induced by crowders also occur in solutions containing fluorescently labeled Ficoll (Figure 2H). Moreover, some of these p53 condensates exhibit localized fluorescence (Figure 2I). Because solutions of Ficoll free of p53 are uniformly bright (Figure 2G), this result affirms that Ficoll is captured in some of the p53 condensates.

The behaviors of the p53 condensates in both crowded and uncrowded solutions conform to the predictions of the model of anomalous protein liquid. With regard to p53, this model implies that the condensates represent p53 species diffusing toward the condensate core, where they associate into transient misassembled oligomers. In turn, the misassembled oligomers diffuse out of the condensates and decay into stable p53 species. These dynamics are illustrated in Figure 2J.

Maturation of Liquid Condensates by Ostwald Ripening

The surface between two phases accrues excess free energy due to the disparate coordination numbers and degrees of freedom of the molecules in the respective phases (Gibbs, 1876, 1993). The surface free energy may dominate the behaviors of phases consisting of multiple nanoscale domains, such as the anomalous liquid revealed in Figures 1 and 2, in which the molecules at the interface represent a significant fraction of the total phase mass. To establish whether the surface free energy of the condensate regulates its characteristics, we monitored the evolution of the condensate population during incubation at 15°C in solutions crowded with Ficoll (Figure 3A). We observed that the condensate radius R increased as a power law of time, $t^{0.30\pm0.10}$ (Figure 3B), whereas the number of condensates N decreased roughly proportionally to the elapsed time (Figure 3C). To exclude that the evolutions of R and N are due to condensate transformation into amyloid fibrils, we characterized the structural integrity of the protein in the anomalous liquid using the ANS assay. The ANS fluorescence of p53 solutions without or with Ficoll exhibited constant intensity over 4 h (Figure 3C inset), and the average value (0.1–0.12) was less than 15% of that of fibrillar aggregates. This finding confirms that p53 is stable at low temperatures, in accordance with the stability observed using DLS (Figures 1F and 1G), and that Ficoll does not destabilize the p53 conformation.

The evolutions of the p53 condensate size and number (Figures 3B and 3C) are a signature of Ostwald ripening of the domains of a disperse phase close to equilibrium with its environment (Lifshitz and Slyozov, 1961). Ostwald ripening is driven by the higher stability of larger domains due to the lower relative contribution of the surface free energy. The less stable smaller domains discharge molecules that diffuse and associate to larger condensates (Figure 3D).

p53 Fibrils Nucleate within p53 Liquid Condensates

Formation of amyloid fibrils of wild-type and mutant p53 is a distinguishing behavior of this protein *in vivo* and *in vitro* (Ano Bom et al., 2012; Wang and Fersht, 2015; Xu et al., 2011). To probe p53 fibrillation, we incubated p53 solutions at 37°C without and with Ficoll and tested the fibrillar nature of the assembled aggregates using ThT. The fluorescence emission of ThT at 488 nm considerably increases upon binding to β-sheet stacks common in amyloid fibrils. Micrographs of p53 aggregates without (Figure 4A) or with (Figure 4B) Ficoll revealed that p53 forms fibrillar structures at 37°C independent of the presence of crowder.

To test whether the fibrillar structures incorporate Ficoll, we incubated fluorescently labeled Ficoll with p53 at 37°C for ca. 6 h, until aggregation was complete. The micrograph of p53-free solution (Figure 4C) displayed homogeneous fluorescence, whereas Ficoll-p53 mixtures exhibited significant heterogeneity of the fluorescent label (Figure 4D) demonstrating that, similar to anomalous p53 liquid condensates, these fibrillar aggregates contain Ficoll. To test the coexistence of anomalous liquid and aggregates in the fibrillar structures, we probed whether the p53 fibrils display constant solubility (Figure 4E). Unlike amyloid fibrils, which exhibit a constant concentration in equilibrium with a fibril polymorph (Qiang et al., 2013), the final p53 concentration after fibrillation increased monotonically with the initial concentration (Figure 4E). A quasi-exponential increase of the captured p53 amount with higher p53 concentration (Figures 1I and 2D) is an intrinsic property of the anomalous p53 liquid. Thus the variable solution concentration at equilibrium with the fibrillar structures implies that they represent a co-condensate of amyloid fibrils and anomalous liquid.

The coexistence of anomalous liquid and fibrils suggests that p53 fibrils may nucleate within p53 liquid condensates. To test this hypothesis, we investigated the effect of Ficoll on the kinetics of fibrillation of p53.

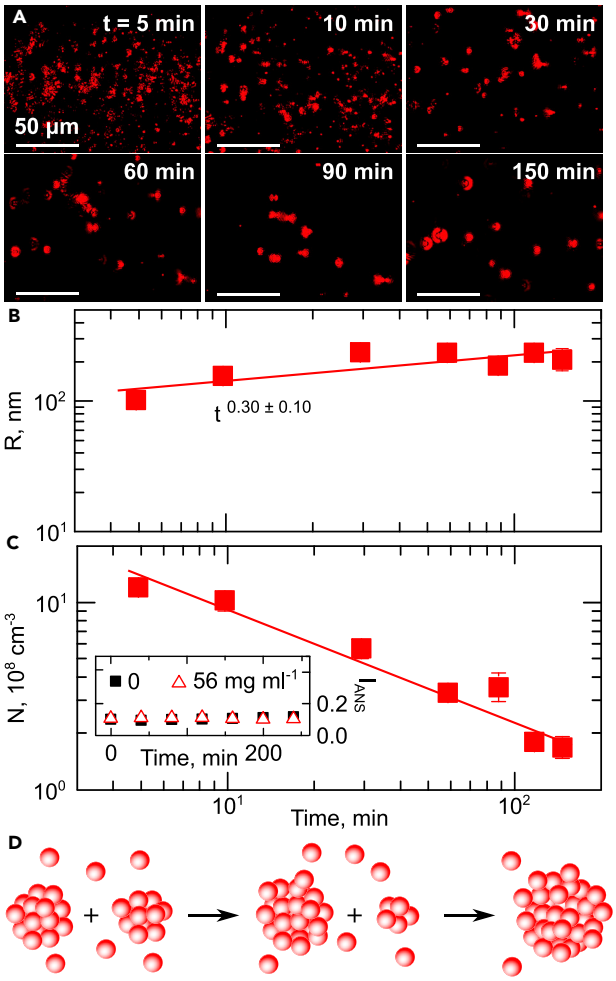

Figure 3. Maturation of the Liquid Condensates

(A) Representative OIM images collected after incubation times indicated in the images. The observed volume is 5 × 80 × 120 μm^3. Condensates appear as red spots. T = 15°C. C_0 = 1.2 μM. C_{Ficoll} = 56 mg mL^{-1}.

(B and C) (B) The average radius *R* and (C) the number density *N* of the condensates as a function of time, corresponding to (A). The average of five determinations in distinct solution volumes is shown. Error bars indicate standard deviations. Inset in (C): normalized fluorescence emission at 500 nm of 7.7 μM p53 solution in the presence of 100 μM ANS and the indicated concentrations of Ficoll. T = 15°C. The emission intensity is normalized to the maximum value observed in the presence of fibrillar aggregates.

(D) Schematic of Ostwald ripening, whereby smaller condensates dissolve, whereas larger condensates grow.

Time-dependent ANS fluorescence revealed that p53 solution lacking crowders exhibited a lag phase, corresponding to fibril nucleation, of ca. 40 min (Figure 4F), somewhat longer than previously reported (Ano Bom et al., 2012; Wang and Fersht, 2015; Wilcken et al., 2012). We tentatively attribute this extension to higher pH, employed here, and the avoidance of Zn^{2+}-binding buffer components, which stabilizes the structure and delays fibrillation. Surprisingly, p53 solutions containing Ficoll evinced significantly longer lag phases (Figure 4F). This observation is counterintuitive because the excluded volume effects of Ficoll and the associated boost of the p53 chemical potential μ_1 would spur fibril nucleation (Ellis and Minton, 2003). The faster fibril growth in crowded solutions, manifest as steeper gain of ANS fluorescence after the lag phase (Figure 4F), concurs with crowding-induced μ_1 increase. Suppressed nucleation in the presence of Ficoll coheres with nuclei assembly hosted within the anomalous liquid condensates. The Ficoll entrapped in the anomalous liquid (Figures 2H–2J) may hinder the motions of the p53 molecules en route to a nucleus. Notably, the observed delay in fibril nucleation due to the segregation of Ficoll in the liquid may be specific to the selected crowder. In this scenario, the accelerated fibril growth in the presence of Ficoll suggests that after nucleation the fibrils emerge from the liquid condensates and grow in the p53 solution.

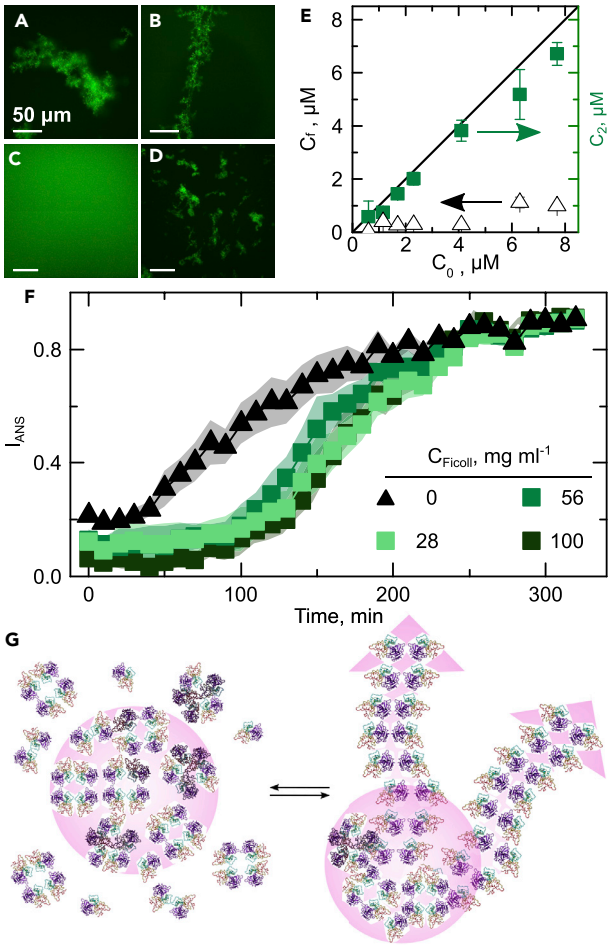

Figure 4. p53 Fibrillation

(A and B) Representative fluorescence micrograph of p53 fibrils formed by incubation at 37°C over 12 h decorated with thioflavin T (ThT); (A) without Ficoll and (B) in the presence of 56 mg mL^{-1} Ficoll. The ThT and p53 concentrations are 200 μM and 7.7 μM, respectively.

(C and D) Representative fluorescence micrographs of 56 mg mL^{-1} fluorescently labeled Ficoll; (C) no protein and (D) in the presence of 7.7 μM p53 after incubation at 37°C over 12 h.

(E) Concentration of p53 after incubation at 37°C in the presence of 56 mg mL^{-1} Ficoll as a function of the initial solution concentration C_0. Δ, the concentration of p53 solution C_f after filtration to remove aggregates. ■, concentration C_2 of p53 incorporated into aggregates, evaluated as $C_2 = C_0 - C_f$. Error bars indicate standard deviations of three measurements on one sample.

(F) Evolution of the intensity of fluorescence at 500 nm of ANS in the presence of p53 at Ficoll concentrations listed on the plot at 37°C. Error bars indicate standard deviations of two measurements on one sample. The p53 and ANS concentrations are 6.5 ± 0.5 and 200 μM, respectively.

(G) Schematic of fibril nucleation within anomalous p53 liquid condensates, followed by growth via sequential association of monomers from the solution.

The mechanism of non-classical fibril nucleation assisted by anomalous p53 liquid, followed by classical growth, is illustrated in Figure 4G.

DISCUSSION

The anomalous p53 liquid condensates identified here share several characteristics with the dense liquids observed with other proteins (Shin and Brangwynne, 2017; Uversky, 2017; Wei et al., 2017). Their formation is reversible, and they are in equilibrium with the solution. They form at solution concentrations as low as 1 μM and capture up to 80% of the protein mass; both parameters are lower by ca. 1,000-fold than with anomalous liquid condensates of folded proteins (Gliko et al., 2005; Schubert et al., 2017; Sleutel

and Van Driessche, 2014; Vorontsova et al., 2015a; Yamazaki et al., 2017). The presence of large disordered regions in the structure is viewed as a prerequisite for conventional liquid condensation at micromolar concentrations (Feric et al., 2016; Shin and Brangwynne, 2017; Uversky, 2017; Wei et al., 2017). In analogy, we conjecture that the low p53 concentration driving anomalous condensation and the large p53 fraction captured in the anomalous condensates are due to the disordered TAD and PRR of p53.

Importantly, the anomalous liquid condensates of p53 are distinct from dense liquid droplets. The defining features of the anomalous condensates are the independence of their size on the solution thermodynamic parameters, including the p53 concentration, and the variable solution concentration at equilibrium.

During maturation, the size of the anomalous liquid condensates evolves following a ca. 1/3 exponent with time, a signature of Ostwald ripening (Lifshitz and Slyozov, 1961). Maturation by Ostwald ripening has been demonstrated for both anomalous and regular protein-dense liquid condensates (Li et al., 2012; Shah et al., 2004). The condensate growth law following a ca. 1/3 exponent with time signifies that the fractal dimension of the p53-dense liquid is close to three (Streitenberger and Förster, 1991), i.e., the condensates are compact objects and not loose molecular assemblies. Furthermore, the finding of condensate maturation by Ostwald ripening highlights the significance of surface free energy for the condensate behaviors.

The fast formation of anomalous liquid condensates and their reversibility may underlie a potential role of the anomalous condensates as loci for storage and protection of p53 (Saad et al., 2017). The condensates may represent a fibril-independent pathway to oncogenicity: unidentified pre-nuclear aggregates of two p53 mutants (R282W and R100P) were shown to accumulate the tumor suppressors p63 and p73 (Xu et al., 2011). In this respect, the p53 liquid condensates may be akin to other protofibrillar assemblies known to trigger disease (Lansbury and Lashuel, 2006).

Similar to other amyloid structures, the formation of p53 fibrils starts with nucleation, whereby local fluctuations of the p53 concentration result in a region of concentrated and ordered p53 molecules with sufficiently unfolded DBDs to allow the assembly of a stacked β-sheet array; this array serves as nucleus for the growth of a fibril (Kashchiev et al., 2013). The creation of a nucleus encounters significant free energy barriers due to the emergence of a surface dividing the fibril from the solution (Gibbs, 1876, 1878, 1993; Kashchiev, 2000). Hence, successful nucleation events are extremely rare. Recent advances in understanding protein phase transitions have demonstrated that nucleation is dramatically faster if the formation of a concentrated protein region precedes ordering (ten Wolde and Frenkel, 1997); this conclusion has been cast as the two-step nucleation mechanism (Kashchiev et al., 2005; Pan et al., 2005; Vekilov, 2010; Vorontsova et al., 2015b). The anomalous protein liquid condensates have been identified as regions of high protein concentration that serve as precursors and facilitators of ordering into structured nuclei of crystals and sickle hemoglobin polymers (Galkin et al., 2007; Sleutel and Van Driessche, 2014; Uzunova et al., 2010; Yamazaki et al., 2017). Theoretical analyses predict that a similar mechanism would apply to the nucleation of amyloid fibrils (Saric et al., 2014); experimental evidence is scarce (Krishnan and Lindquist, 2005; Lansbury and Lashuel, 2006). Careful tests should examine the validity of the two-step nucleation scenario for each protein forming amyloid structures of interest (Auer et al., 2012).

Nucleation of p53 amyloid fibrils within anomalous p53 liquid resolves several mysteries of p53 aggregation kinetics. The uncommon independence of the nucleation rate constants of p53 concentration (Wang and Fersht, 2017; Wilcken et al., 2012) may be due to nucleation housed in anomalous liquid, in which the p53 concentration may be constant. The contradictory results on cross-seeding of p63 and p73 aggregation with p53 fibrils (Ano Bom et al., 2012; Wang and Fersht, 2015; Xu et al., 2011) may be due to the coexistence of fibrils and anomalous liquid and the distinct proportions that each aggregate class occupies in independently prepared seeds.

The strong dependence of the volume of the anomalous liquid phase on the p53 concentration suggests that the anomalous condensates could be sensitively controlled by modifying the concentration of free p53, for instance, by the negative regulators MDM2 and MDMX. MDM2 and MDMX cooperate with ubiquitinate p53, resulting in nuclear export and proteasomal degradation in the cytosol (Wade et al., 2013). MDMX inhibits p53 directly, by binding to the TAD of p53 (Popowicz et al., 2008). The consequences of ubiquitination and nuclear export on liquid condensation are modeled by lowering the concentration of

p53. In addition, MDMX binding to the disordered TAD region induces folding (Joerger and Fersht, 2016). As the presence of large disordered regions in the p53 structure may be a prerequisite for anomalous liquid condensation at micromolar concentrations, it is feasible that that MDMX may strongly suppress anomalous liquid condensation.

Cancer-associated p53 mutations are concentrated in the DBD (Joerger and Fersht, 2008). They are broadly subdivided into contact mutations that remove essential DNA interaction sites and structural mutations that perturb the structure of the ordered DBD, thereby reducing its kinetic and thermodynamic stability (Joerger and Fersht, 2008, 2016). The enhanced aggregation of the structurally destabilized mutants and the associated oncogenic GOF has been supported by numerous experiments *in vitro* and in cell culture (Costa et al., 2016; Freed-Pastor et al., 2012; Joerger and Fersht, 2008, 2016; Rajagopalan et al., 2011; Wang and Fersht, 2017; Wilcken et al., 2012; Xu et al., 2011), whereas the contact mutations R273H, R273C, R248W, which preserve the protein conformation, raise additional unsettled questions. The dominant-negative effects of R273H and R248W, where arginines at sites 273 and 248 are replaced with, respectively, histidine and tryptophan (Ano Bom et al., 2012; Joerger and Fersht, 2016), have been attributed to the formation of hybrid p53 tetramers with the wild-type allele (Xu et al., 2011), which lowers the concentration of active p53. No mechanism, however, has been proposed for the suppression of the p63 and p73 function, and this void is hard to reconcile with the severity of cancers associated with the binding mutations (Seagle et al., 2015). The finding of anomalous liquid condensates that host fibril nucleation suggests that the enhanced aggregation of missense p53 mutants with preserved conformational stability may be due to enhanced condensate formation. Indeed, the amount of the anomalous liquid phase is governed by the intermolecular interactions in the solution, quantified as the second virial coefficient B_2. In turn, altering the charge of the protein by substituting a positive side chain with a neutral one significantly enhances intermolecular attraction and the magnitude of B_2.

In cells, p53 localizes in the nucleus, in which DNA, protein complexes, RNAs and multiple other types of biomolecules occupy up to 50% of the total volume. To mimic crowding, we employ Ficoll, a cross-linked polysaccharide. Although the fraction of the solution volume occupied by the crowder is representative of the intracellular environment, the distribution of the charges on the surface of the Ficoll molecules may diverge from that of densely charged molecules like DNA, RNA, and proteins. Hence the observed delay in fibril nucleation due to the segregation of Ficoll in the condensates may be specific to the selected crowder. It helped to elucidate a crucial aspect of the fibril nucleation mechanism, but it may be immaterial to intracellular p53 aggregation.

We demonstrate a dramatic boost in anomalous liquid volume induced by crowding, which may signify a strong correlation between macromolecular crowding and the rates and degree of p53 fibrillation *in vivo*. Such correlation provides a mechanistic link between the increase in cancer frequency and the decreases in cellular and tissue hydration in the aged (Hatters et al., 2002; Popkin et al., 2010). As the loss of cellular water is equivalent to a larger fraction of cellular volume occupied by macromolecules, our results suggest that accelerated p53 aggregation with advancing age is due to the increased macromolecular crowding.

Limitations of the Study

Our study clearly demonstrates the presence of dense liquid condensates in solutions of p53. These condensates exhibit several anomalous properties that distinguish them from the typical protein condensates, such as crystals, amyloid fibrils, and dense liquids. The anomalous properties of the condensates observed in p53 solutions highlight their similarity to the mesoscopic clusters observed in solutions of several proteins and studied in depth in the last 10 years owing to their role as precursors for the nucleation of ordered protein solids. Two behaviors distinguish the anomalous p53 condensates from the mesoscopic clusters: they form at concentrations lower by about 1,000× and they capture a significant fraction of the protein in the solution. We tentatively attributed these behaviors to the large disordered region of p53, but this correlation needs to be theoretically and experimentally examined.

The evidence that the anomalous p53 condensates host the nucleation of p53 amyloid fibrils, while solid, is indirect. Direct imaging, perhaps by liquid-phase electron microscopy, could provide definitive data.

METHODS

All methods can be found in the accompanying Transparent Methods supplemental file.

SUPPLEMENTAL INFORMATION

Supplemental Information includes Transparent Methods, five figures, and two videos and can be found with this article online at https://doi.org/10.1016/j.isci.2019.01.027.

ACKNOWLEDGMENTS

We thank Dominique Maes, Frederic Rousseau, Joost Schymkowitz, and Navin Varadarajan for valuable discussions of p53 aggregation, protein conformational stability, and protein expression and translocation. Sabine Petry graciously provided materials support for experiments. This work was supported by grants from NASA (NNX14AD68G and NNX14AE79G), NSF (MCB-1518204, DMR-1710354, and DMR-1131155), and the Welch Foundation (E-1869).

AUTHOR CONTRIBUTIONS

A.B.K. and P.G.V conceived this work. J.C.C. and P.G.V. directed the research. Z.W. prepared the plasmid and expressed the protein. K.T and M.S.S. purified the protein. M.S.S. characterized p53 aggregation. M.S.S., P.G.V., and J.C.C. analyzed the data. A.B.K. and P.G.V. developed theory. P.G.V., M.S.S., and J.C.C. wrote the paper.

DECLARATION OF INTERESTS

The authors declare no competing interests.

Received: August 29, 2018
Revised: January 3, 2019
Accepted: January 16, 2019
Published: February 22, 2019

REFERENCES

Aguzzi, A., and O'Connor, T. (2010). Protein aggregation diseases: pathogenicity and therapeutic perspectives. Nat. Rev. Drug Discov. *9*, 237–248.

Ang, H.C., Joerger, A.C., Mayer, S., and Fersht, A.R. (2006). Effects of common cancer mutations on stability and DNA binding of full-length p53 compared with isolated core domains. J. Biol. Chem. *281*, 21934–21941.

Ano Bom, A.P.D., Rangel, L.P., Costa, D.C.F., de Oliveira, G.A.P., Sanches, D., Braga, C.A., Gava, L.M., Ramos, C.H.I., Cepeda, A.O.T., Stumbo, A.C., et al. (2012). Mutant p53 aggregates into prion-like amyloid oligomers and fibrils: implications for cancer. J. Biol. Chem. *287*, 28152–28162.

Asherie, N., Pande, J., Lomakin, A., Ogun, O., Hanson, S.R., Smith, J.B., and Benedek, G.B. (1998). Oligomerization and phase separation in globular protein solutions. Biophys. Chem. *75*, 213–227.

Auer, S., Ricchiuto, P., and Kashchiev, D. (2012). Two-step nucleation of amyloid fibrils: omnipresent or not? J. Mol. Biol. *422*, 723–730.

Bell, S., Klein, C., Müller, L., Hansen, S., and Buchner, J. (2002). p53 contains large unstructured regions in its native state. J. Mol. Biol. *322*, 917–927.

Berne, B., and Pecora, R. (2000). Dynamic Light Scattering with Applications to Chemistry, Biology, and Physics (Dover).

Bieging, K.T., Mello, S.S., and Attardi, L.D. (2014). Unravelling mechanisms of p53-mediated tumour suppression. Nat. Rev. Cancer *14*, 359–370.

Broide, M.L., Berland, C.R., Pande, J., Ogun, O.O., and Benedek, G.B. (1991). Binary liquid phase separation of lens proteins solutions. Proc. Natl. Acad. Sci. U S A *88*, 5660–5664.

Chaikin, P.M., and Lubensky, T.C. (1995). Principles of Condensed Matter Physics (Cambridge Unversity Press).

Chalkey, G.E., Knowles, P.P., Whitehead, P.C., and Coffer, A.I. (1994). Biochemical characterisation of purified human wild-type p53 overexpressed in insect cells. Eur. J. Biochem. *221*, 167–175.

Chan, Ho Y., Lankevich, V., Vekilov, Peter G., and Lubchenko, V. (2012). Anisotropy of the Coulomb interaction between folded proteins: consequences for mesoscopic aggregation of lysozyme. Biophys. J. *102*, 1934–1943.

Chen, Q., Vekilov, P.G., Nagel, R.L., and Hirsch, R.E. (2004). Liquid-liquid separation in hemoglobins: distinct aggregation mechanisms of the β6 mutants. Biophys. J. *86*, 1702–1712.

Chernov, A.A., and Komatsu, H. (1995). Principles of crystal growth in protein crystallization. In Science and Technology of Crystal Growth, J.P. van der Eerden and O.S.L. Bruinsma, eds. (Kluwer Academic), pp. 329–353.

Costa, D.C.F., de Oliveira, G.A.P., Cino, E.A., Soares, I.N., Rangel, L.P., and Silva, J.L. (2016). Aggregation and prion-like properties of misfolded tumor suppressors: is cancer a prion disease? Cold Spring Harb. Perspect. Biol. *8*, a023614.

Ellis, R.J., and Minton, A.P. (2003). Cell biology: join the crowd. Nature *425*, 27–28.

Fabry, M.E., Desrosiers, L., and Suzuka, S.M. (2001). Direct intracellular measurement of deoxygenated hemoglobin S solubility. Blood *98*, 883–884.

Feric, M., Vaidya, N., Harmon, T.S., Mitrea, D.M., Zhu, L., Richardson, T.M., Kriwacki, R.W., Pappu, R.V., and Brangwynne, C.P. (2016). Coexisting liquid phases underlie nucleolar subcompartments. Cell *165*, 1686–1697.

Freed-Pastor, William A., Mizuno, H., Zhao, X., Langerød, A., Moon, S.-H., Rodriguez-Barrueco, R., Barsotti, A., Chicas, A., Li, W., Polotskaia, A., et al. (2012). Mutant p53 disrupts mammary tissue architecture via the mevalonate pathway. Cell *148*, 244–258.

Galkin, O., Chen, K., Nagel, R.L., Hirsch, R.E., and Vekilov, P.G. (2002). Liquid-liquid separation in solutions of normal and sickle cell hemoglobin. Proc. Natl. Acad. Sci. U S A *99*, 8479–8483.

Galkin, O., Pan, W., Filobelo, L., Hirsch, R.E., Nagel, R.L., and Vekilov, P.G. (2007). Two-step mechanism of homogeneous nucleation of sickle cell hemoglobin polymers. Biophys. J. *93*, 902–913.

Georgalis, Y., Philipp, M., Aleksandrova, R., and Krüger, J.K. (2012). Light scattering studies on Ficoll PM70 solutions reveal two distinct diffusive modes. J. Colloid Interface Sci. *386*, 141–147.

Gibbs, J.W. (1876). On the equilibrium of heterogeneous substances, First Part. Trans. Conn. Acad. Arts Sci. *3*, 108–248.

Gibbs, J.W. (1878). On the equilibrium of heterogeneous substances (concluded). Trans. Conn. Acad. Arts Sci. *3*, 343–524.

Gibbs, J.W. (1993). The Scientific Papers of J.W. Gibbs. Volume One Thermodynamics (Oxbow Press).

Gliko, O., Neumaier, N., Pan, W., Haase, I., Fischer, M., Bacher, A., Weinkauf, S., and Vekilov, P.G. (2005). A metastable prerequisite for the growth of lumazine synthase crystals. J. Am. Chem. Soc. *127*, 3433–3438.

Gogna, R., Madan, E., Kuppusamy, P., and Pati, U. (2012). Re-oxygenation causes hypoxic tumor regression through restoration of p53 wild-type conformation and post-translational modifications. Cell Death Dis. *3*, e286.

Hatters, D.M., Minton, A.P., and Howlett, G.J. (2002). Macromolecular crowding accelerates amyloid formation by human apolipoprotein C-II. J. Biol. Chem. *277*, 7824–7830.

Hawe, A., Sutter, M., and Jiskoot, W. (2008). Extrinsic fluorescent dyes as tools for protein characterization. Pharm. Res. *25*, 1487–1499.

Joerger, A.C., and Fersht, A.R. (2008). Structural biology of the tumor suppressor p53. Annu. Rev. Biochem. *77*, 557–582.

Joerger, A.C., and Fersht, A.R. (2016). The p53 pathway: origins, inactivation in cancer, and emerging therapeutic approaches. Annu. Rev. Biochem. *85*, 375–404.

Kashchiev, D. (2000). Nucleation. Basic Theory with Applications (Butterworth, Heinemann).

Kashchiev, D., Cabriolu, R., and Auer, S. (2013). Confounding the paradigm: peculiarities of amyloid fibril nucleation. J. Am. Chem. Soc. *135*, 1531–1539.

Kashchiev, D., Vekilov, P.G., and Kolomeisky, A.B. (2005). Kinetics of two-step nucleation of crystals. J. Chem. Phys. *122*, 244706.

Kato, G.J., Piel, F.B., Reid, C.D., Gaston, M.H., Ohene-Frempong, K., Krishnamurti, L., Smith, W.R., Panepinto, J.A., Weatherall, D.J., Costa, F.F., et al. (2018). Sickle cell disease. Nat. Rev. Dis. Primers *4*, 18010.

Knowles, T.P.J., Vendruscolo, M., and Dobson, C.M. (2014). The amyloid state and its association with protein misfolding diseases. Nat. Rev. Mol. Cell Biol. *15*, 384–396.

Krishnan, R., and Lindquist, S.L. (2005). Structural insights into a yeast prion illuminate nucleation and strain diversity. Nature *435*, 765–772.

Lansbury, P.T., and Lashuel, H.A. (2006). A century-old debate on protein aggregation and neurodegeneration enters the clinic. Nature *443*, 774–779.

Li, Y., Lubchenko, V., Vorontsova, M.A., Filobelo, L., and Vekilov, P.G. (2012). Ostwald-like ripening of the anomalous mesoscopic clusters in protein solutions. J. Phys. Chem. B *116*, 10657–10664.

Lifshitz, I.M., and Slyozov, V.V. (1961). The kinetics of precipitation from supersaturated solid solutions. J. Phys. Chem. Solids *19*, 35–50.

Muller, P.A.J., and Vousden, K.H. (2013). p53 mutations in cancer. Nat. Cell Biol. *15*, 2–8.

Muschol, M., and Rosenberger, F. (1997). Liquid-liquid phase separation in supersaturated lysozyme solutions and associated precipitate formation/crystallization. J. Chem. Phys. *107*, 1953–1962.

Olivier, M., Eeles, R., Hollstein, M., Khan, M.A., Harris, C.C., and Hainaut, P. (2002). The IARC TP53 database: new online mutation analysis and recommendations to users. Hum. Mutat. *19*, 607–614.

Pan, W., Galkin, O., Filobelo, L., Nagel, R.L., and Vekilov, P.G. (2007). Metastable mesoscopic clusters in solutions of sickle cell hemoglobin. Biophys. J. *92*, 267–277.

Pan, W., Kolomeisky, A.B., and Vekilov, P.G. (2005). Nucleation of ordered solid phases of protein via a disordered high-density state: phenomenological approach. J. Chem. Phys. *122*, 174905.

Pan, W., Vekilov, P.G., and Lubchenko, V. (2010). The origin of anomalous mesoscopic phases in protein solutions. J. Phys. Chem. B *114*, 7620–7630.

Popkin, B.M., D'Anci, K.E., and Rosenberg, I.H. (2010). Water, hydration and health. Nutr. Rev. *68*, 439–458.

Popowicz, G., Czarna, A., and Holak, T. (2008). Structure of the human Mdmx protein bound to the p53 tumor suppressor transactivation domain. Cell Cycle *7*, 2441–2443.

Qiang, W., Kelley, K., and Tycko, R. (2013). Polymorph-specific kinetics and thermodynamics of β-amyloid fibril growth. J. Am. Chem. Soc. *135*, 6860–6871.

Rajagopalan, S., Huang, F., and Fersht, A.R. (2011). Single-Molecule characterization of oligomerization kinetics and equilibria of the tumor suppressor p53. Nucleic Acids Res. *39*, 2294–2303.

Saad, S., Cereghetti, G., Feng, Y., Picotti, P., Peter, M., and Dechant, R. (2017). Reversible protein aggregation is a protective mechanism to ensure cell cycle restart after stress. Nat. Cell Biol. *19*, 1202–1213.

Safari, M.S., Byington, M.C., Conrad, J.C., and Vekilov, P.G. (2017). Polymorphism of lysozyme condensates. J. Phys. Chem. B *121*, 9091–9101.

Saric, A., Chebaro, Y.C., Knowles, T.P.J., and Frenkel, D. (2014). Crucial role of nonspecific interactions in amyloid nucleation. Proc. Natl. Acad. Sci. U S A *111*, 17869–17874.

Sasaki, M., Nie, L., and Maki, C.G. (2007). MDM2 binding induces a conformational change in p53 that is opposed by heat-shock protein 90 and precedes p53 proteasomal degradation. J. Biol. Chem. *282*, 14626–14634.

Schubert, R., Meyer, A., Baitan, D., Dierks, K., Perbandt, M., and Betzel, C. (2017). Real-time observation of protein dense liquid cluster evolution during nucleation in protein crystallization. Cryst. Growth Des. *17*, 954–958.

Seagle, B.-L.L., Eng, K.H., Dandapani, M., Yeh, J.Y., Odunsi, K., and Shahabi, S. (2015). Survival of patients with structurally-grouped TP53 mutations in ovarian and breast cancers. Oncotarget *6*, 18641–18652.

Shah, M., Galkin, O., and Vekilov, P.G. (2004). Smooth transition from metastability to instability in phase separating protein solutions. J. Chem. Phys. *121*, 7505–7512.

Shin, Y., and Brangwynne, C.P. (2017). Liquid phase condensation in cell physiology and disease. Science *357*, https://doi.org/10.1126/science.aaf4382.

Sleutel, M., and Van Driessche, A.E. (2014). Role of clusters in nonclassical nucleation and growth of protein crystals. Proc. Natl. Acad. Sci. U S A *111*, E546–E553.

Soragni, A., Janzen, D.M., Johnson, L.M., Lindgren, A.G., Nguyen, A.T.-Q., Tiourin, E., Soriaga, A.B., Lu, J., Jiang, L., Faull, K.F., et al. (2016). A designed inhibitor of p53 aggregation rescues p53 tumor-suppression in ovarian carcinomas. Cancer Cell *29*, 90–103.

Streitenberger, P., and Förster, D. (1991). The effect of surface fractal dimension of particles on Ostwald ripening. Phys. Status Solidi B Basic Solid State Phys. *164*, K65–K68.

ten Wolde, P.R., and Frenkel, D. (1997). Enhancement of protein crystal nucleation by critical density fluctuations. Science *277*, 1975–1978.

Thomson, J.A., Schurtenberger, P., Thurston, G.M., and Benedek, G.B. (1987). Binary liquid phase separation and critical phenomena in a protein water solution. Proc. Natl. Acad. Sci. U S A *84*, 7079–7083.

Uversky, V.N. (2017). Intrinsically disordered proteins in overcrowded milieu: membrane-less organelles, phase separation, and intrinsic disorder. Curr. Opin. Struct. Biol. *44*, 18–30.

Uzunova, V.V., Pan, W., Galkin, O., and Vekilov, P.G. (2010). Free heme and the polymerization of sickle cell hemoglobin. Biophys. J. *99*, 1976–1985.

van den Berg, J., Boersma, A.J., and Poolman, B. (2017). Microorganisms maintain crowding homeostasis. Nat. Rev. Microbiol. *15*, 309.

van Raaij, M.E., van Gestel, J., Segers-Nolten, I.M.J., de Leeuw, S.W., and Subramaniam, V. (2008). Concentration dependence of α-synuclein fibril length assessed by quantitative atomic force microscopy and statistical-mechanical theory. Biophys. J. *95*, 4871–4878.

Vekilov, P.G. (2010). Nucleation. Cryst. Growth Des. *10*, 5007–5019.

Vorontsova, M.A., Chan, H.Y., Lubchenko, V., and Vekilov, P.G. (2015a). Lack of dependence of the sizes of the mesoscopic protein clusters on electrostatics. Biophys. J. *109*, 1959–1968.

Vorontsova, M.A., Maes, D., and Vekilov, P.G. (2015b). Recent advances in the understanding of two-step nucleation of protein crystals. Faraday Discuss. *179*, 27–40.

Wade, M., Li, Y.-C., and Wahl, G.M. (2013). MDM2, MDMX and p53 in oncogenesis and cancer therapy. Nat. Rev. Cancer *13*, 83–96.

Wang, G., and Fersht, A.R. (2015). Propagation of aggregated p53: cross-reaction and coaggregation vs. seeding. Proc. Natl. Acad. Sci. U S A *112*, 2443–2448.

Wang, G., and Fersht, A.R. (2017). Multisite aggregation of p53 and implications for drug rescue. Proc. Natl. Acad. Sci. U S A *114*, E2634–E2643.

Wei, M.-T., Elbaum-Garfinkle, S., Holehouse, A.S., Chen, C.C.-H., Feric, M., Arnold, C.B., Priestley, R.D., Pappu, R.V., and Brangwynne, C.P. (2017). Phase behaviour of disordered proteins underlying low density and high permeability of liquid organelles. Nat. Chem. *9*, 1118–1125.

Wilcken, R., Wang, G., Boeckler, F.M., and Fersht, A.R. (2012). Kinetic mechanism of p53 oncogenic mutant aggregation and its inhibition. Proc. Natl. Acad. Sci. U S A *109*, 13584–13589.

Xu, J., Reumers, J., Couceiro, J.R., De Smet, F., Gallardo, R., Rudyak, S., Cornelis, A., Rozenski, J., Zwolinska, A., Marine, J.-C., et al. (2011). Gain of function of mutant p53 by coaggregation with multiple tumor suppressors. Nat. Chem. Biol. *7*, 285–295.

Yamazaki, T., Kimura, Y., Vekilov, P.G., Furukawa, E., Shirai, M., Matsumoto, H., Van Driessche, A.E.S., and Tsukamoto, K. (2017). Two types of amorphous protein particles facilitate crystal nucleation. Proc. Natl. Acad. Sci. U S A *114*, 2154–2159.

ISCI, Volume *12*

Supplemental Information

Anomalous Dense Liquid Condensates Host the Nucleation of Tumor Suppressor p53 Fibrils

Mohammad S. Safari, Zhiqing Wang, Kunaal Tailor, Anatoly B. Kolomeisky, Jacinta C. Conrad, and Peter G. Vekilov

SUPPLEMENTAL FIGURES

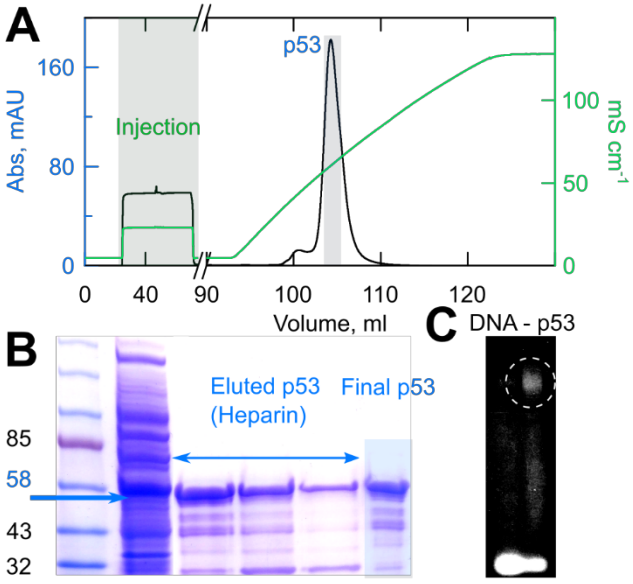

Figure S1. Purification and identification of p53. Related to Figure 1. **A.** Absorbance at 280 nm and conductivity of a p53 solution eluting from a heparin resin chromatography column using a 2 M NaCl gradient. **B.** Characterization of chromatography fractions by SDS PAGE. Columns: 1, molecular weight standards; 2, soluble fractions of lysed whole cells; 3 - 5, chromatography fractions from **A**, 3 corresponds to the fraction highlighted in blue; 6, purified p53 after desalting. **C.** Electrophoretic mobility shift assay (EMSA). Lane 1, 399 ng consensus DNA; lane 2, 7 μM p53 + 599 ng consensus DNA. Lane 2 demonstrates impeded DNA mobility due to binding to p53.

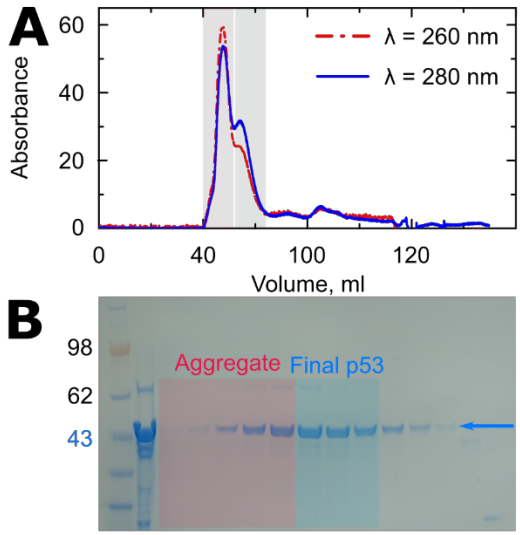

Figure S2. Optimized purification of p53. Related to Figure 1. **A.** Absorbance at 260 and 280 nm of a p53 solution eluting from size exclusion 16/600 Superdex 200 column. **B.** Characterization of chromatography fractions by SDS PAGE. Columns: 1, molecular weight standards: 2, soluble fractions of lysed whole cells; 3 – 7, chromatography fractions highlighted in red in **A**; 8 – 10, chromatography fractions highlighted in blue in **A**, representing solution used in tests illustrated in Figure S3**;** columns 11 – 13, discarded fractions.

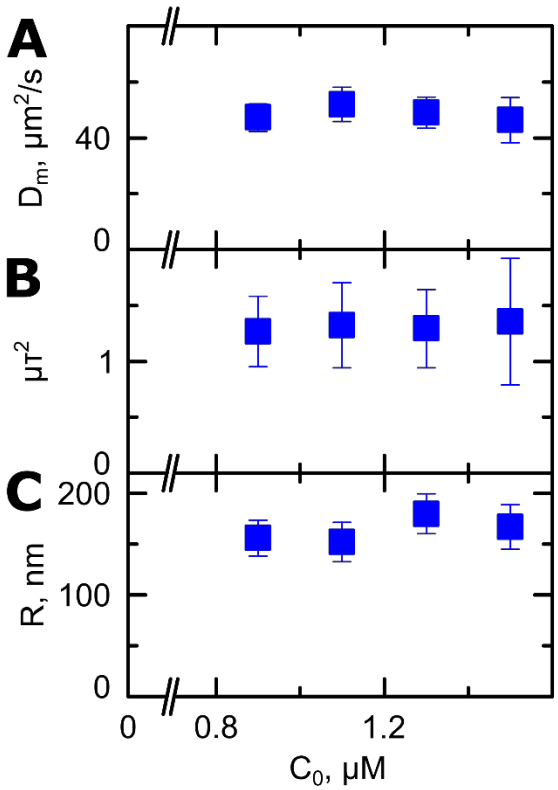

Figure S3. Characterization of the unaggregated protein and the anomalous liquid condensates in solutions of p53 purified using size exclusion chromatography. Related to Figure 1. **A, B.** Dependencies of diffusivity D_m and dispersity $\mu\tau^2$ of unaggregated p53 measured at 15°C by dynamic light scattering as in Figure 1G. The error bars are generated from four distinct determinations. **C.** The dependence of the average radius R of the anomalous liquid condensates at 37°C on the protein concentration C_0 measured using dynamic light scattering as in Figure 1L. The error bars are generated from four distinct determinations.

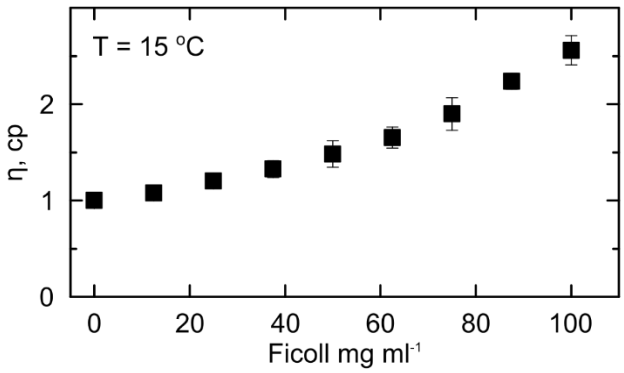

Figure S4. The viscosity η of Ficoll solution with concentrations ranging 0 to 100 mg ml^{-1} determined from the diffusivity of polystyrene spheres of known size monitored by dynamic lights scattering. Related to Figure 2.

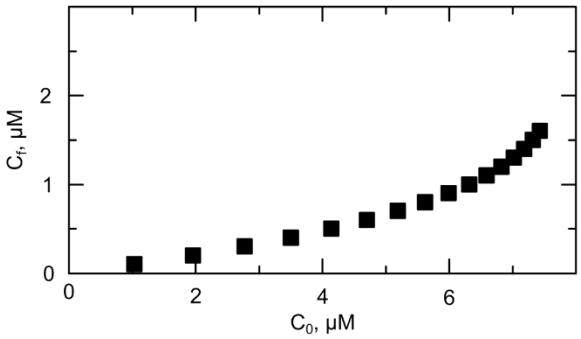

Figure S5. The correlation between the concentration C_f of the solution in equilibrium with the mesoscopic p53-rich condensates and the total concentration C_0 of p53 in the solution evaluated from $C_2 = C_f \exp\left(-\frac{\psi_2 - \mu_1^0}{RT}\right) \exp(2B_2 M_w C_f)$ and $C_0 = C_f + C_2$, where C_2 is the p53 amount captured in the condensates. Related to Figure 2.

TRANSPARENT METHODS

Oblique illumination microscopy. We detected and characterized p53 aggregates using oblique illumination microscopy (OIM) (Li et al., 2011); this method is also referred to as Brownian microscopy or particle tracking (Filipe et al., 2010; Li et al., 2011; Maes et al., 2015a; Vorontsova et al., 2015). In this method, a green laser illuminates a thin solution layer at an oblique angle such that the incident beam avoids the lens of a microscope positioned above the sample (Li et al., 2011). This method enables the detection of nano- and microscale objects through light scattered at wavevectors of order μm^{-1}. The scattered intensity is proportional to the sixth power of the scatterers' sizes; thus, in a solution containing objects of varying size the scattering signal is dominated by larger particles. This feature makes this technique particularly well suited to characterize the size and number distribution of the aggregates that appear as bright cyan spots in OIM micrographs (Figure 1C).

We used a Nanosight LM10-HS microscope (Nanosight Ltd). Solutions were loaded into a thermostatically controlled cuvette of volume ~ 0.3 ml and depth 0.5 mm. The illumination wavelength was 532 nm. We used a 20× lens (NA. 0.4). A sensitive CMOS camera supplied by Nanosight Ltd was used to record a movie of condensates undergoing Brownian motion. The rate of acquisition was about 25 fps. Each frame of the movie was an image of condensates as bright spots on a dark background. The accompanying software package was used to determine the center of these spots in each frame of the movie and build contiguous condensate trajectories. The condensate diffusivity was obtained from the slope of the dependence of the mean-squared displacement as a function of lag time. The condensate radius R_c was evaluated from the Stokes-Einstein equation using viscosity values determined using dynamic light scattering as discussed below. The number of condensate spots in a frame (using the focal depth of 5 μm, $V_{Scattering} = 120 \times 80 \times 5\ \mu m^{-3}$) yielded the condensate concentration (Maes et al., 2015b; Vorontsova et al., 2015; Vorontsova et al., 2016). Movies were acquired over 30 seconds. We found that objects recorded for times shorter than 1 s were interference spots from two or more condensates tracked for significantly longer times. This observation was supported by the estimate that a condensate with diffusivity $D_2 \approx 10^{-12}\ m^2 s^{-1}$ would be detectable in a focal plane with depth 5 μm for about 25 s. Therefore, we excluded these short-duration objects from the determination of the condensate parameters. Five movies from distinct solution volumes were collected in each tested sample. The numbers of condensates in each range of sizes were averaged.

Dynamic light scattering (DLS). DLS data were collected using an ALV instrument (ALV-GmbH, Langen, Germany), which consisted of an ALV goniometer, a He-Ne laser (wavelength λ = 632.8 nm), and an ALV-5000/EPP Multiple tau Digital Correlator. Normalized intensity-intensity correlation functions $g_2(q,\tau)$ of duration 45 seconds were recorded over monitored time span at a fixed scattering angle of 90°. From intensity-intensity correlation functions that possess one shoulder we determined the characteristic diffusion time τ and polydispersity index $\mu\tau^2$ of the p53 solution by fitting the normalized correlation function with a polydisperse exponential fit (Safari et al., 2017; Safari et al., 2015):

$$g_2(q,\tau) - 1 = \left(A \exp\left(-\tau/\tau_m\right)(1 + \mu\tau^2/2)\right)^2 + \varepsilon(\tau) \quad (1)$$

where A is the scattering amplitude, which is proportional to the intensity scattered by the species in the solution, and $\varepsilon(\tau)$ accounts for mechanical, optical, and electronic noise in the signal (Li et

al., 2011; Pan et al., 2007). In our measurements, ε was one or two orders of magnitude lower than the amplitudes. We used τ_m to determine the average diffusivity, D_m, from $D_m = (q^2\tau)^{-1}$, where $q = \frac{4\pi n}{\lambda}\sin(\theta/2)$ is the wave vector at a scattering angle of 90°, λ = 632.8 nm is the wavelength of the incident red laser and n = 1.33 is the solution refractive index (Byington et al., 2016; Vorontsova et al., 2015).

From intensity-intensity correlation functions with two distinct shoulders, we determined the characteristic diffusion times τ_m and τ_c of the monomers and condensates by fitting with a squared sum of exponentials (Li et al., 2011; Safari et al., 2017; Safari et al., 2015)

$$g_2(q,\tau) - 1 = \left(A_m \exp\left(-\tau/\tau_m\right)(1 + \mu_m \tau^2/2) + A_f \exp\left(-\tau/\tau_c\right)\right)^2 + \varepsilon(\tau) \qquad (2)$$

where A_m and A_f are amplitudes proportional to the intensity scattered by the monomers and condensates, respectively, and $\varepsilon(\tau)$ accounts for mechanical, optical, and electronic noise in the signal (Li et al., 2011; Pan et al., 2007). We used τ_m and τ_c to determine the monomer and condensate diffusivities, D_m and D_c, from $D_m = (q^2\tau_m)^{-1}$ and $D_c = (q^2\tau_c)^{-1}$, where $q = \frac{4\pi n}{\lambda}\sin(\theta/2)$ is the scattering wave vector at 90°.

From the diffusivities D_m and D_c we computed the average size R of monomers and condensates from the Stokes-Einstein relation, $R_i = \frac{k_B T}{6\pi\eta D_i}$. Here T, k_B, and η are respectively the temperature, Boltzmann constant, and the viscosity of the solution. The buffer viscosity η_i was determined from the dynamics of 2 μm-diameter Fluoro-Max Dyed Red Fluorescent polystyrene spheres diffusing in the buffer solution, as characterized by DLS (Pan et al., 2007). Viscosities of the buffer with 10% glycerol without Ficoll at 15 and 37 °C were 1.50 ± 0.05 and 0.95 ± 0.03 mPa·s, respectively (Figure S4).

Static light scattering to characterize p53-p53 interactions. Osmotic compressibility was measured with the ALV instrument, discussed above. We measured the intensity scattered at 90° from p53 solutions with protein concentration varying from 0.12 – 0.4 mg mL^{-1} in incubation buffer: 50 mM Tris at pH = 7.85, 150 mM NaCl, 10% glycerol, and 5 mM TCEP. The average molecular weight M_w and the second virial coefficient B_2 were calculated from the plot of KC_0/R_θ as a function of p53 concentration C_0 following (Berne and Pecora, 2000; Pan et al., 2010)

$$KC_0/R_\theta = M_w^{-1} + 2B_2C_0 \qquad (3)$$

Here $R_\theta = I_\theta/I_0$ is the Rayleigh ratio of scattered to incident intensity and K is the system constant, defined as $K = N_A^{-1}\left(\frac{2\pi n}{\lambda^2}\right)^2\left(\frac{dn}{dc}\right)^2$ (Berne and Pecora, 2000), where n = 1.33 is the refractive index of the solvent and dn/dc = 0.20 is the first derivative of the refractive index with respect to protein concentration. dn/dc was measured using a Brookhaven Instruments differential refractometer operating at a wavelength of 620 nm (Pan et al., 2010).

Protein expression and purification. Plasmid pET15b-TP53 was transformed into *E. coli* BL21 (DE3). A single colony of the fresh transformants was inoculated into 10 mL media containing 20 g L^{-1} Bacto-trypton, 10 g L^{-1} yeast extract, 5 g L^{-1} NaCl, and 100 μg mL^{-1} ampicillin. The culture was grown for 5 hours and the seed culture was then diluted by a factor of 100 into 1 L of the same media. When the optical density measured at 600 nm of the subculture reached 0.4 – 0.5, the cells were cold-shocked on ice for 25 minutes, induced by 0.1 mM IPTG (β-D-1-

thiogalactopyranoside) and 0.2 mM $ZnCl_2$, and the culture was let grow at 20 °C at 250 rpm overnight (Bell et al., 2002; Wong et al., 1999).

The cells were pelleted and re-suspended in 100 mM KH_2PO_4/K_2HPO_4 (pH = 8.0), 300 mM NaCl, 5% glycerol, and 2 mM TCEP (2 mL per 1 g of wet cells) to a final volume of 40 mL. 1 mL of 10x EDTA free protease inhibitor cocktail (SIGMA FAST protease inhibitor tablets) was added to the cell suspension. The suspension was then aliquoted into 4 mL fractions in 5 mL Eppendorf tubes for sonication to lyse the cells. Each aliquot was thrice sonicated using a Q-SONICA MISONIX XL-2000 (11 watt output) for 30 seconds on ice with 15 min intervals between sonications. The lysate was then centrifuged at 5000 rpm for 1 h to pellet the cell mass. The supernatant was filtered with 0.45 μm SFCA syringe filters prior to purification.

For purification, Ni Sepharose™ 6 Fast Flow column was equilibrated with 100 mM KH_2PO_4/K_2HPO_4 at pH = 8.0, 300 mM NaCl, 5% glycerol, 2 mM TCEP, and 25 mM imidazole. Bound p53 was eluted with a linear gradient of imidazole. Fractions containing p53 were diluted 1:1 with 20 mM KH_2PO_4/K_2HPO_4 at pH = 6.50, 5% (v/v) glycerol, and 5 mM TCEP for further binding to HiTrap™ Heparin HP column. p53 bound to this column was eluted with a linear gradient of NaCl (Figure S1A). The purified p53 was further buffer exchanged using GE healthcare PD-10 desalting columns to 50 mM Tris at pH = 7.85, 150 mM NaCl, 5 mM TCEP, and 10% glycerol for storage and experiments. After buffer exchange, the p53 stock solution was flash frozen in liquid nitrogen and stored in aliquots of ~15 μM at –80 °C. The yield of soluble p53, with final purity of ~85% after all steps (Figure S1B), was about ~1.5 mg per 1 L of medium (Bell et al., 2002).

Solutions were prepared from aliquots thawed on ice. Thawed protein and incubation buffer, 50 mM Tris at pH = 7.85, 150 mM NaCl, 5 mM TCEP, 10% glycerol, were filtered with 0.22 μm Polyethersulfone (PES) syringe filters prior to all measurements. The concentration of stock p53 solution was determined by absorbance measurements using a Beckman Coulter Du 800 spectrophotometer and extinction coefficient ε = 0.763 mL $mg^{-1}cm^{-1}$ at 280 nm (Bell et al., 2002; Gill and von Hippel, 1989).

Alternative protein purification method using size exclusion chromatography. To optimize the purity of final wt-p53 from bacteria expression system, we cloned the p53 insert into a different pET vector containing a N-terminus GFP with GSSG linker connected to p53. The GFP-p53 plasmid was then transformed into Rosetta™2(DE3)pLysS competent cells. A single colony of the fresh transformants was inoculated into 10 mL media containing 20 g L^{-1} Bacto-trypton, 10 g L^{-1} yeast extract, 10 g L^{-1} NaCl, 100 μg mL^{-1} Carbenicillin, and 25 μg mL^{-1} chloramphenicol. The culture was grown for 5-6 hours and the seed culture was then diluted by a factor of 100 into to 2 L of the same media containing 0.2 mM ZnCl2. When the optical density measured at 600 nm of the subculture reached 0.4 – 0.5, the cells were cold-shocked on ice for 25 minutes, induced by 1 mM IPTG (β-D-1-thiogalactopyranoside) and the culture was let grow at 20 °C at 180 rpm overnight (Bell et al., 2002; Wong et al., 1999).

The cells were pelleted and re-suspended in 50 mM Tris, 200 mM KCl, 500 mM NaCl, (pH = 8.0), 5% glycerol, 5 mM β-Mercaptoethanol, and 20 mM Imidazole (2 mL per 1 g of wet cells) to a final volume of 40 mL. 1 mL of 10× EDTA-free protease inhibitor cocktail (SIGMA FAST protease inhibitor tablets) was added to the cell suspension. The cells were then lysed by French press. The lysate was centrifuged at 15,000 rpm for 1 h to pellet the cell mass.

For purification, Ni SepharoseTM 6 Fast Flow column was equilibrated with 50 mM Tris, 200 mM KCl, 500 mM NaCl, (pH = 8.0), 5% glycerol, and 5 mM β-Mercaptoethanol, and 20 mM Imidazole. Bound GFP-p53 was eluted with 500 mM imidazole. Fractions containing GFP-p53 (green) were diluted 1:10 with 20 mM KH2PO4/K2HPO4 at pH = 6.00, 5% (v/v) glycerol, and 5 mM TCEP for further binding to HiTrapTM Heparin HP column. The bound GFP- p53 was eluted with a linear gradient of NaCl. The purified p53 was then injected into size exclusion 16/600 Superdex 200 column increase equilibrated with 50 mM Tris at pH = 7.85, 150 mM NaCl, 5 mM TCEP, and 10% glycerol as the final step of purification. This step removes majority of the contaminants, yielding a protein with more than 99% purity. The yield of soluble GFP-p53 was 0.9 mg per 1L media.

We replicated the above protocol with pET-wt-p53 vector (purchased from Addgene). After size exclusion, we obtained the wt-p53 (no tag) with more than 90% purity (using Image J densitometry, the estimated purity is 91-92%, Figure S2 A and B). The purified p53 stock solution was flash frozen in liquid nitrogen and stored in aliquots of ~60 μM at –80 °C. The yield of soluble p53 was 0.4 mg per 1L media.

Dynamic light scattering measurements (Figures S3 A and B) demonstrate that the diffusion coefficient of the unaggregated protein purified by size exclusion chromatography (SEC) is higher than that of the protein purified using a heparin column. The average diffusivity D_m =43 $\mu m^2 s^{-1}$ (Figure S3A) relates (by the Stokes-Einstein law $D_m = k_B T/6\pi\eta R_m$, where $k_B T$ is the thermal energy, η = 1.5 mPa·s is independently measured solvent viscosity and R_m is the molecular hydrodynamic radius) to an average R_m = 4.4 nm, similar to the ca. 4 nm radius expected for a p53 tetramer of molecular weight 175 kg mol^{-1} (Chalkey et al., 1994). The solution polydispersity $\mu\tau^2 \approx 1.4$ (Figure S3B) is significantly enhanced, compared to solutions purified using heparin columns, which exhibit $\mu\tau^2 \approx 0.35$ (Figure 1G), indicating increased fraction of high-order oligomers. This observation suggests that SEC destabilizes p53 tetramers, possibly owing to the high shear rates associated with the complex hydrodynamics of SEC systems (Barth and Carlin, 1984).

Solutions purified by size exclusion chromatography contain aggregates of size ca. 160 nm, which is independent of the p53 concentration (Figure S3C). The concentration independence of their size is a signature behavior of the anomalous liquid condensates. The condensate radius is similar to that of the anomalous condensates observed in solutions purified using heparin column. The two latter observations suggest that the selection of the purification method does not affect the formation of the anomalous liquid condensates in p53 solutions and the condensates observed in Figures 1 – 3 are an intrinsic property of p53, whose behaviors are not impacted by the solution impurities.

Solutions. We monitored the aggregation of p53 in solutions in 50 mM Tris buffer at pH = 7.85 in the presence of 150 mM NaCl, 5 mM TCEP, and 10% glycerol. We avoided the often-used phosphate buffer since it may precipitate Zn^{2+} ions, which stabilize the protein conformation (Butler and Loh, 2007), as insoluble phosphates. The selected pH was preserved from the last purification step and is somewhat higher than the value of 7.20 used in other investigations of *in vitro* p53 aggregation (Ano Bom et al., 2012; Wilcken et al., 2012). This pH shift does not destabilize the conformation of wild-type p53 (DiGiammarino et al., 2001); on the contrary, the chosen pH is further separated from the protein isoelectric point pI = 6.83 (Chalkey et al., 1994), at which the p53 molecules are neutral and their assembly is amplified owing to suppressed electrostatic repulsion. We expect the molecular charge attained at pH higher than the pI to

impede aggregation (Cohn and Edsall, 1943; Pace et al., 2009) and expose the pertinent mechanisms.

Characterization of unaggregated solutions. To remove possible aggregates, p53 solutions were filtered with 0.22 μm Polyethersulfone (PES) syringe filters. The average size and polydispersity of the scatterers were characterized by dynamic light scattering as discussed above.

Mimicking macromolecular crowding. As a crowding agent, we chose Ficoll 70 kDa, a cross-linked compact polysaccharide with radius 4.7 nm (Georgalis et al., 2012). As alternatives, we considered Dextran and polyethylene glycol (PEG). Dextran, a branched polymer, was rejected since it forms entangled structures that modify molecular transport at moderate and elevated concentrations (Carrasco et al., 1989). Our OIM tests revealed that PEG solutions are inhomogeneous due to suspended particles or PEG aggregates. Importantly, determinations of the concentration of unaggregated p53 in equilibrium with the condensates, which are independent of the crowder heterogeneity, in the presence of PEG and Ficoll, respectively, yielded identical results. To reduce the number of condensates to within a range accessible by OIM, we performed these tests at 15°C. Ficoll was added to the p53 solutions at desired concentration as a stock solution at 250 mg mL^{-1} with 200 mM NaCl in DI-water 20 min after preparation of solutions; this solution retains the ionic strength of the buffer holding p53.

Fluorescence labeling of Ficoll. Ficoll was activated with chloroacetate at pH>13 for 4 hours, followed by addition of hydrazine in presence of EDAC (N-(3-Dimethylaminopropyl)-N′-ethylcarbodiimide hydrochloride) to prepare amine-activated Ficoll (Inman, 1975; Milley et al., 2016). This derivative was treated with Fluorescein in presence of EDAC to generate Fluorescein-labeled Ficoll. The product was dialyzed against 2 L DI-water for 1 week with regular daily exchange of the water. The dialysate was concentrated using 10k Amicon centrifuge filters followed by an additional buffer exchange step using a desalting PD-10 column to eliminate any residual free dye. The eluted Ficoll was then filtered with 0.2 μm PTFE (Polytetrafluoroethylene) syringe filter and the filtrate was concentrated to 100 mg mL^{-1} using an Amicon 10k filter. An extinction coefficient of 2.00 ± 0.12 × 10^{-3} mL mg^{-1} cm^{-1} at 280 nm was used to determine the Ficoll concentration, which was evaluated independently by measuring absorbance of duplicate solutions of 164 mg mL^{-1} of un-labeled Ficoll.

To determine whether Ficoll incorporated into p53 fibrils, p53 concentration was set at 7.7 μM in presence of 56 mg mL^{-1} fluorescein-labelled Ficoll and the solution was incubated at 37 °C over 12 hours to form large aggregates. Control samples were prepared with same content of labeled Ficoll without p53. 10 μL of samples were placed on a large cover slip (48 mm × 65 mm, Fisherbrand), covered with a smaller cover slip (22 mm × 22 mm, Fisherbrand), and placed on the stage of an 00999epi-fluorescence microscope (Leica DM 3000B) equipped with a 40× objective lens (NA. 0.65). Images were collected using a sCMOS camera (pco.edge 4.2, field of view 212.5 × 213.3) from four distinct locations of the samples under excitation wavelength of 488 nm.

To determine whether Ficoll incorporated into mesoscopic p53-rich condensates, amine-activated Ficoll solution was reacted with NHS-ester BODIPY/530 and BODIPY labeled-Ficoll was buffer exchanged and concentrated as mentioned above to final concentration of 30 mg mL^{-1} Ficoll. This solution was incubated at 15°C in the Nanosight cuvette for 2 h. First, a movie of 10 seconds was collected without any filter cube in the optical path. Within 1 min after the end of this movie, the fluorescence filter cube was inserted into the optical path and a fluorescence movie

was collected for 10 s. Assuming a diffusion coefficient of D = 1 μm² s^{-1} for condensates in presence of Ficoll, the approximate displacement of the condensates was < 6 μm ($\Delta x = \sqrt{D\Delta t}$), so that the condensates remained within the field of view over the 30 s duration of an experiment. Comparison of fluorescence movie with the OIM image reveals the p53 condensates that contain BODIPY-Ficoll inside. The control movie with no p53 confirms that these condensates were not formed by labeled Ficoll.

ANS and ThT assays for characterization of p53 fibrillation kinetics. The fibrillation kinetics of p53 was characterized at 37 °C using a 1-anilino-8-naphthalenesulfonate (ANS) assay (Frare et al., 2009; Hawe et al., 2008; Munishkina and Fink, 2007). ANS was dissolved at a concentration of 18 mM in incubation buffer, 50 mM Tris at pH = 7.85, 150 mM NaCl, 5 mM TCEP, 10 % glycerol. The solution was filtered through a 0.2 μm Teflon filter. The ANS concentration was determined spectrophotometrically using extinction coefficient 18 mM^{-1} cm^{-1} at 270 nm (Hawe et al., 2008). For experimental statistics, two identical samples of each solution mixture were loaded in a 96-well plate and the fluorescence response to excitation at 350 nm was recorded at an emission wavelength of 500 nm by an Infinite 200 PRO microplate reader (Tecan) at 10 minute intervals over six hours.

Thioflavin T (ThT) was dissolved at 20 mM in incubation buffer: 50 mM Tris at pH = 7.85, 150 mM NaCl, 5 mM TCEP, 10% glycerol. The ThT concentration was determined spectrophotometrically using extinction coefficient 26.6 mM^{-1}cm^{-1} at 416 nm (Biancalana and Koide, 2010; Hawe et al., 2008). To test the fibrillar nature of the aggregates, a p53 solution at concentration of 7.7 μM was incubated with 0 and 56 mg mL^{-1} Ficoll at T = 37 °C for 12 hours to form large aggregates. The aggregates were then pelleted using centrifugation at 14,000 rpm for 20 minutes. The pellet was re-suspended in 100 μL of the incubation buffer and 1 μL of stock ThT solution was added to the suspension. After 20 minutes of incubation, 10 μL of samples were imaged as described in above.

Rendering the structure of p53. Full length structure of p53 was generated by inputting the FASTA sequence in PHYRE2 algorithm available online using intensive mode. 82% of the residues are modelled with more than 90% confidence. Residues 96-354 (DBD and OD) are modelled using p53 template in PDB with 100% confidence (Joerger and Fersht, 2008; Kelley et al., 2015). Tetramer structure drawn as suggested in (Okorokov and Orlova, 2009).

Reagents. TCEP (tris(2-carboxyethyl)phosphine, 8-Anilinonaphthalene-1-sulfonic acid (ANS), Thioflavin T (ThT), Ficoll PM-70, and Fluorescein were purchased from Sigma Aldrich. EDAC. N-(3-Dimethylaminopropyl)-N′-ethylcarbodiimide hydrochloride and BODIPY-530/550 NHS ester were purchased from Thermo Fisher Scientific. For wild-type p53, the plasmid pET15b-TP53, containing N-terminal 6–his–WT–p53 (1–393), was purchased from Addgene (Ayed et al., 2001).

The equilibrium between the mesoscopic p53-rich condensates and the solution. We first demonstrate that the correlation between the concentration C_f of the solution in equilibrium with the mesoscopic p53-rich condensates and the total concentration of p53 in the solution C_o in Figures 1I and 2D is incompatible with 1. Chemical equilibrium between p53 molecules in solution and modified molecules that form condensates. 2. Equilibrium between p53 in the solution and solid p53 aggregates. 3. Equilibrium between p53 in the solution and in a stable dense liquid phase. Lastly, we derive a correlation between the C_f and C_o for mesoscopic p53-rich condensates in equilibrium with the solution.

1. Chemical equilibrium between p53 molecules in solution and condensates composed of modified molecules. We assume that p53 transforms to another form that assembles into condensates. Let C_o be the total concentration of p53 in the solution, C_f the concentration of intact p53 in equilibrium with the modified form, and C_2 the concentration of modified p53.

The chemical potential μ_1 of p53 in the final solution is

$$\mu_1 = \mu_1^o + RT \ln C_f + RT \ln \gamma_1$$

where RT is the universal gas constant, T is temperature, and γ is the activity coefficient.

The chemical potential of the modified form μ_2 is

$$\mu_2 = \mu_2^0 + RT \ln C_2 + RT \ln \gamma_2$$

where γ_2 is the activity coefficient of the modified p53, and $C_f\gamma_1 = a_1$ and $C_2\gamma_2 = a_2$ are the respective activities.

At equilibrium $\mu_1 = \mu_2$ and

$$\frac{a_2}{a_1} = \exp[-(\mu_2^0 - \mu_1^0)/RT] \equiv K$$

where K is the equilibrium constant. For the ratio, C_f/C_o we obtain

$$\frac{C_f}{C_0} = \frac{C_f}{C_f + C_2} \cong \frac{1}{1+K}$$

The approximate equality is satisfied if $\gamma_1 \approx \gamma_2$. The latter relation indicates that C_f is proportional to C_o, $C_f = (1+K)^{-1}C_i$.

2. Equilibrium between p53 in the solution and solid p53 aggregates. *Again,*

$$\mu_1 = \mu_1^o + RT \ln C_f + RT \ln \gamma_1$$

Since the concentration of the solid is constant, in this case

$$\mu_2 = \mu_2^0 = \text{const}$$

We obtain

$$\mu_1^o + RT \ln C_f + RT \ln \gamma_1 = \mu_2^0 = \text{const}$$

where $RT \ln \gamma_1 = 2B_2 M_w C_f RT$, B_2 is the second osmotic virial coefficient, and M_w is the p53 molecular weight. With the value of B_2 = -1.1×10^{-3} mol m^{3}kg^{-2} determined from the Debye plot in Figure 2E, the function on the left-hand side is a monotonically increasing function of C_f for $C_f <$ 20 μM. Hence, the above equality has a single solution for C_f, which represents the solubility of the solid p53 aggregates, i.e., C_f is independent of C_o.

3. Equilibrium between p53 in the solution and a stable dense liquid phase. According to the Landau model of phase equilibria, equilibria between two coexisting phases are described by $\mu(C)$ dependences that exhibit a decreasing segment bracketed by two increasing branches.

A $\mu(C)$ dependence similar to the $\mu_1(C_f)$ relation accounting for B_2 above corresponds to a monotonically increasing μ for low concentrations, followed by a monotonically decreasing branch. To obtain the wave required by the Landau model, we need to account for an additional member in the virial expansion of μ.

$$\mu = \mu^0 + RT \ln C + 2B_2 M_w C + 3B_3 M_w^2 C^2$$

There exist an infinite number of pairs of concentrations that satisfy the condition that chemical potentials in the two phases in equilibrium are equal, $\mu_1 = \mu_2$. The corresponding $\mu(C)$ points are located along the two respective increasing branches of the $\mu(C)$ wave. Only one pair (C_f, C_{DL}), however, satisfies the equilibrium condition $\Delta G = 0$. Since

$$\Delta G = \int_{C_f}^{C_{DL}} [\mu(C) - \mu(C_f)] dC \,,$$

the pair (C_f, C_{DL}) is found employing the Maxwell construction that ensures that the area between the horizontal line at $\mu(C_f) = \mu(C_{DL})$ and the $\mu(C)$ wave is equal to zero.

This result indicates that C_f is independent of the initial concentration of the solution before liquid-liquid demixing, C_o.

4. The correlation between C_f and C_o for mesoscopic p53-rich condensates. The deviation of the $C_f(C_0)$ correlations in Figures 1I and 2D from the predictions of the three models discussed above suggest that the condensates of p53 represent a unique phase, distinct from dense liquid, solid aggregates, or aggregates of chemically modified species. Notably, several behaviors of the p53 condensates are similar to those of the mesoscopic protein-rich condensates observed in solutions of several proteins: condensate size independent of the concentrations of both protein and crowder, and evolution of the condensate population akin to Ostwald ripening.

These similarities suggest that the p53 condensates might form following a mechanism similar to the one found for the protein-rich condensates. In application to p53, the condensate formation mechanism would assume the association of misassembled p53 oligomers, distinct from the biologically active p53 tetramers. The presence of misassembled oligomers is suggested by the significant polydispersity of the p53 solution, the exaggerated size of the unaggregated p53, and the average molecular weight of ca. 303 kDa, determined by static light scattering; the latter value is about double the 160 kDa expected for the tetramers.

Assuming that the condensates are in equilibrium with the solution imposes equality of the chemical potentials of the p53 tetramers in the condensates to that in the solution,

$$\mu_2 = \mu_1$$

The presence of other species in the condensates suggests that $\mu_2^0 \neq \mu_1^0$. Furthermore, the p53 tetramers in the condensates experience nonideality that is not captured by the B_2 member in the $\mu_1(C)$ expression above. Importantly, assuming that the concentration of tetramers in the condensates is constant and independent of their concentration in the solution, this contribution to μ_2 would be constant. We designate the modified standard chemical potential of the p53 in the condensates as ψ_2. We account for the increasing number of condensates at higher solution concentration by introducing an entropy term $RT \ln C_2$, where C_2 corresponds to the total amount

of protein captured in the condensates. The expression for the chemical potential of p53 in the condensates becomes

$$\mu_2 = \psi_2 + RT \ln C_2$$

With

$$\mu_1 = \mu_1^0 + RT \ln C_f + 2B_2 M_w C_f RT$$

we obtain

$$C_2 = C_f \exp\left(-\frac{\psi_2 - \mu_1^0}{RT}\right) \exp\left(2B_2 M_w C_f\right)$$

This expression complies with the correlation between C_f and C_2 in Figure 2F. Numerical solution presented in Figure S5 demonstrates a quasi-exponential correlation between C_f and C_o, corresponding to the experimental determinations in Figures 1I and 2D.

SUPPLEMENTAL REFERENCES

Ano Bom, A.P.D., Rangel, L.P., Costa, D.C.F., de Oliveira, G.A.P., Sanches, D., Braga, C.A., Gava, L.M., Ramos, C.H.I., Cepeda, A.O.T., Stumbo, A.C.*, et al.* (2012). Mutant p53 Aggregates into Prion-like Amyloid Oligomers and Fibrils: IMPLICATIONS FOR CANCER. The Journal of Biological Chemistry *287*, 28152-28162.

Ayed, A., Mulder, F.A.A., Yi, G.-S., Lu, Y., Kay, L.E., and Arrowsmith, C.H. (2001). Latent and active p53 are identical in conformation. Nature Structural Biology *8*, 756.

Barth, H.G., and Carlin, F.J. (1984). A Review of Polymer Shear Degradation in Size-Exclusion Chromatography. Journal of Liquid Chromatography *7*, 1717-1738.

Bell, S., Klein, C., Müller, L., Hansen, S., and Buchner, J. (2002). p53 contains large unstructured regions in its native state. J Mol Biol *322*, 917-927.

Berne, B., and Pecora, R. (2000). Dynamic Light Scattering with Applications to Chemistry, Biology, and Physics (Mineola, NY: Dover).

Biancalana, M., and Koide, S. (2010). Molecular Mechanism of Thioflavin-T Binding to Amyloid Fibrils. Biochimica et biophysica acta *1804*, 1405-1412.

Butler, J.S., and Loh, S.N. (2007). Zn2+-Dependent Misfolding of the p53 DNA Binding Domain. Biochemistry *46*, 2630-2639.

Byington, M.C., Safari, M.S., Conrad, J.C., and Vekilov, P.G. (2016). Protein Conformational Flexibility Enables the Formation of Dense Liquid Clusters: Tests Using Solution Shear. The Journal of Physical Chemistry Letters *7*, 2339-2345.

Carrasco, F., Chornet, E., Overend, R.P., and Costa, J. (1989). A generalized correlation for the viscosity of dextrans in aqueous solutions as a function of temperature, concentration, and molecular weight at low shear rates. Journal of Applied Polymer Science *37*, 2087-2098.

Chalkey, G.E., Knowles, P.P., Whitehead, P.C., and Coffer, A.I. (1994). Biochemical characterisation of purified human wild-type p53 overexpressed in insect cells. European Journal of Biochemistry *221*, 167-175.

Cohn, E.J., and Edsall, J.T. (1943). PROTEINS, AMINO ACIDS AND PEPTIDES AS IONS AND DIPOLAR IONS (New York: REINHOLD PUBLISHING CORPORATION).

DiGiammarino, E.L., Lee, A.S., Cadwell, C., Zhang, W., Bothner, B., Ribeiro, R.C., Zambetti, G., and Kriwacki, R.W. (2001). A novel mechanism of tumorigenesis involving pH-dependent destabilization of a mutant p53 tetramer. Nature Structural Biology *9*, 12.

Filipe, V., Hawe, A., and Jiskoot, W. (2010). Critical Evaluation of Nanoparticle Tracking Analysis (NTA) by NanoSight for the Measurement of Nanoparticles and Protein Aggregates. Pharmaceutical Research *27*, 796-810.

Frare, E., Mossuto, M.F., de Laureto, P.P., Tolin, S., Menzer, L., Dumoulin, M., Dobson, C.M., and Fontana, A. (2009). Characterization of Oligomeric Species on the Aggregation Pathway of Human Lysozyme. Journal of Molecular Biology *387*, 17-27.

Georgalis, Y., Philipp, M., Aleksandrova, R., and Krüger, J.K. (2012). Light scattering studies on Ficoll PM70 solutions reveal two distinct diffusive modes. Journal of Colloid and Interface Science *386*, 141-147.

Gill, S.C., and von Hippel, P.H. (1989). Calculation of protein extinction coefficients from amino acid sequence data. Analytical Biochemistry *182*, 319-326.

Hawe, A., Sutter, M., and Jiskoot, W. (2008). Extrinsic Fluorescent Dyes as Tools for Protein Characterization. Pharmaceutical Research *25*, 1487-1499.

Inman, J.K. (1975). Thymus independent antigens: the preparation of covalent, hapten Ficoll conjugates. Journal of Immunology *114*, 704-709.

Joerger, A.C., and Fersht, A.R. (2008). Structural Biology of the Tumor Suppressor p53. Annual Review of Biochemistry *77*, 557-582.

Kelley, L.A., Mezulis, S., Yates, C.M., Wass, M.N., and Sternberg, M.J.E. (2015). The Phyre2 web portal for protein modeling, prediction and analysis. Nature Protocols *10*, 845.

Li, Y., Lubchenko, V., and Vekilov, P.G. (2011). The Use of Dynamic Light Scattering and Brownian Microscopy to Characterize Protein Aggregation. Rev Sci Instrum *82*, 053106

Maes, D., Vorontsova, M.A., Potenza, M.A.C., Sanvito, T., Sleutel, M., Giglio, M., and Vekilov, P.G. (2015a). Do protein crystals nucleate within dense liquid clusters? Acta Crystallographica Section F *71*, 815-822.

Maes, D., Vorontsova, M.A., Potenza, M.A.C., Sanvito, T., Sleutel, M., Giglio, M., and Vekilov, P.G. (2015b). Do protein crystals nucleate within dense liquid clusters? Acta Crystallographica Section F, Structural Biology Communications *71*, 815-822.

Milley, B., Kiwan, R., Ott, G.S., Calacsan, C., Kachura, M., Campbell, J.D., Kanzler, H., and Coffman, R.L. (2016). Optimization, Production, and Characterization of a CpG-Oligonucleotide-Ficoll Conjugate Nanoparticle Adjuvant for Enhanced Immunogenicity of Anthrax Protective Antigen. Bioconjugate Chemistry *27*, 1293-1304.

Munishkina, L.A., and Fink, A.L. (2007). Fluorescence as a method to reveal structures and membrane-interactions of amyloidogenic proteins. Biochimica et Biophysica Acta (BBA) - Biomembranes *1768*, 1862-1885.

Okorokov, A.L., and Orlova, E.V. (2009). Structural biology of the p53 tumour suppressor. Current Opinion in Structural Biology *19*, 197-202.

Pace, C.N., Grimsley, G.R., and Scholtz, J.M. (2009). Protein Ionizable Groups: pK Values and Their Contribution to Protein Stability and Solubility. Journal of Biological Chemistry *284*, 13285-13289.

Pan, W., Galkin, O., Filobelo, L., Nagel, R.L., and Vekilov, P.G. (2007). Metastable mesoscopic clusters in solutions of sickle cell hemoglobin. Biophys J *92*, 267-277.

Pan, W., Vekilov, P.G., and Lubchenko, V. (2010). The origin of anomalous mesoscopic phases in protein solutions. J Phys Chem B *114* 7620-7630.

Safari, M.S., Poling-Skutvik, R., Vekilov, P.G., and Conrad, J.C. (2017). Differential dynamic microscopy of bidisperse colloidal suspensions. npj Microgravity *3*, 21.

Safari, M.S., Vorontsova, M.A., Poling-Skutvik, R., Vekilov, P.G., and Conrad, J.C. (2015). Differential dynamic microscopy of weakly scattering and polydisperse protein-rich clusters. Physical Review E *92*, 042712.

Vorontsova, M.A., Chan, H.Y., Lubchenko, V., and Vekilov, P G. (2015). Lack of Dependence of the Sizes of the Mesoscopic Protein Clusters on Electrostatics. Biophysical Journal *109*, 1959-1968.

Vorontsova, M.A., Vekilov, P.G., and Maes, D. (2016). Characterization of the diffusive dynamics of particles with time-dependent asymmetric microscopy intensity profiles. Soft Matter *12*, 6926-6936.

Wilcken, R., Wang, G., Boeckler, F.M., and Fersht, A.R. (2012). Kinetic mechanism of p53 oncogenic mutant aggregation and its inhibition. Proceedings of the National Academy of Sciences *109*, 13584-13589.

Wong, K.-B., DeDecker, B.S., Freund, S.M.V., Proctor, M.R., Bycroft, M., and Fersht, A.R. (1999). Hot-spot mutants of p53 core domain evince characteristic local structural changes. Proceedings of the National Academy of Sciences of the United States of America *96*, 8438-8442.